

California State University, San Bernardino

CSUSB ScholarWorks

Theses Digitization Project

John M. Pfau Library

2013

Fiducial-free alignment verification techniques for intracranial radiosurgery

Kenneth Matthew Williams

Follow this and additional works at: <https://scholarworks.lib.csusb.edu/etd-project>



Part of the [Radiology Commons](#), and the [Software Engineering Commons](#)

Recommended Citation

Williams, Kenneth Matthew, "Fiducial-free alignment verification techniques for intracranial radiosurgery" (2013). *Theses Digitization Project*. 4225.

<https://scholarworks.lib.csusb.edu/etd-project/4225>

This Thesis is brought to you for free and open access by the John M. Pfau Library at CSUSB ScholarWorks. It has been accepted for inclusion in Theses Digitization Project by an authorized administrator of CSUSB ScholarWorks. For more information, please contact scholarworks@csusb.edu.

FIDUCIAL-FREE ALIGNMENT VERIFICATION TECHNIQUES FOR
INTRACRANIAL RADIOSURGERY

A Thesis
Presented to the
Faculty of
California State University,
San Bernardino

In Partial Fulfillment
of the Requirements for the Degree
Master of Science
in
Computer Science

by
Kenneth Matthew Williams
September 2013

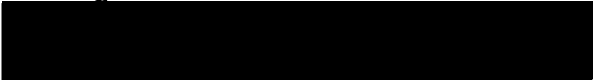
FIDUCIAL-FREE ALIGNMENT VERIFICATION TECHNIQUES FOR
INTRACRANIAL RADIOSURGERY

A Thesis
Presented to the
Faculty of
California State University,
San Bernardino

by
Kenneth Williams

September 2013.

Approved by:


Keith Evan Schubert, Advisor, School of
Computer Science and Engineering


Ernesto Gomez


Arturo Concepcion


Andrew Wroe

Aug 27, 2013
Date

© 2013 Kenneth Matthew Williams

ABSTRACT

Protons are an external beam modality of radiation therapy that can be used effectively for radiosurgical applications due to the dosimetry advantage of the Bragg peak. The Bragg peak is a phenomenon exploited by proton beam therapy to concentrate the effect of the beams on the tumor while minimizing damage to critical structures and other healthy tissue within the patient. The peak in the proton's dose distribution occurs because the interaction cross section increases as the particle's energy and velocity decrease, meaning the proton is more likely to interact with the surrounding particles. To maximize the effectiveness of the Bragg peak, the patient must be properly aligned for accurate targeting of the tumor volume. The current process of intracranial radiosurgery at Loma Linda University Medical Center (LLUMC) utilizes implanted titanium surgical screws in the patient's skull that act as fiducial markers to assist with image guidance for alignment verification. These fiducials add an element of physical and emotional stress to the patient, and the surgery for implantation adds a significant delay before the radiosurgery procedure can begin. During the procedure, the therapist/physician manually aligns the patient to the proton beam isocenter using digital x-ray images and the implanted fiducials and/or fixed bony landmarks visible on these images. This method of alignment can be time-intensive and requires personnel who are specifically trained in patient alignment. This thesis serves as the basis for a method using image registration to automate patient alignment in an effort to eliminate the dependency on the fiducial markers as well as improve the accuracy and efficiency of the alignment process. Several image registration algorithms are analyzed and compared for consideration for further

testing and potential implementation. Given the sensitivity of patient care, these algorithms must fulfill basic requirements for accuracy, robustness, and performance. In this work, digitally reconstructed radiographs from the treatment planning computed tomography (CT) scan of a skull phantom act as the reference images, while digital x-ray images taken in the treatment room represent the captured images to be aligned. This research was conducted under the clinical supervision of Dr. Andrew Wroe and Dr. Reinhard Schulte of LLUMC.

ACKNOWLEDGEMENTS

Nothing of me is original. I am the combined effort of everyone I've ever known. [28]

In light of the above quote, I would first like to thank everyone. If not for everyone with whom I have ever been acquainted, I would not be the person I am as of this writing.

I would like to thank Dr. Keith Schubert, my advisor, for his advice and the technical expertise he has bestowed upon me throughout my research efforts. He has also provided me with further research ideas and the confidence to pursue a doctorate degree in this field. I would like to thank Dr. Reinhard Schulte and Dr. Andrew Wroe for their medical expertise with which I have combined my technical experience to explore new opportunities. The most significant of these opportunities was the ability to contribute to the same hospital at which I was treated for cancer as a child.

I thank each member of my committee, as well as each faculty member at the School of Computer Science and Engineering, for their wisdom and encouragement throughout my academic career at California State University, San Bernardino. I thank Dr. Arturo Concepcion for his guidance and providing me with a vast number of opportunities to enhance my knowledge and experience that have prepared me for my future. I thank Dr. Ernesto Gomez for his lectures in distributed computing, which has proved insightful for how to organize my algorithms.

I thank Tom Lee who has shared his time assisting me with understanding the Digital Imaging and Communications in Medicine (DICOM) medical imaging file format which has allowed me to conduct my research.

I thank my family and friends for the love, support, and encouragement they have provided throughout my life.

DEDICATION

To those who have lost their fight with cancer.

TABLE OF CONTENTS

<i>Abstract</i>	iii
<i>Acknowledgements</i>	v
<i>List of Tables</i>	xi
<i>List of Figures</i>	xii
1. Introduction	1
1.1 Overview	1
1.2 Background	2
1.2.1 Introduction to Stereotactic Radiosurgery	3
1.2.2 Gamma Knife	4
1.2.3 Linear Accelerator Systems	5
1.2.4 Proton Beam Therapy	6
1.3 Purpose	8
1.4 Scope	9
1.5 Definition of Terms and Abbreviations	9
2. Review of the Literature	14
2.1 Introduction to Image Registration	14
2.2 Image Registration in Medical Imaging	16

3. <i>Methods for Image Registration</i>	18
3.1 Introduction	18
3.2 Interpolation	19
3.3 Phase Correlation Using Log-Polar Coordinates	21
3.4 Mutual Information Maximization	24
3.5 Enhanced Correlation Coefficient Maximization	26
3.6 Iterative Closest Point Methods	27
3.6.1 Feature Detection for Point Cloud Generation	28
3.6.2 Nearest Neighbor Search	31
3.7 Log-Domain Diffeomorphic Registration	34
3.8 Partial Differential Equation-Based Methods	34
4. <i>Results and Discussion</i>	37
4.1 Introduction	37
4.2 Comparison of Methods	44
4.3 Comparison of Results	51
5. <i>Summary of Findings</i>	53
5.1 Conclusions	53
5.2 Recommendations for Implementation	55
5.3 Future Research	56
<i>Appendix A: Image Registration Algorithms</i>	57
A.1 Phase Correlation Using Log-Polar Coordinates	58
A.2 Mutual Information Maximization	59
A.3 Enhanced Correlation Coefficient Maximization	60
A.4 Iterative Closest Point Methods	61
A.5 Log-Domain Diffeomorphic Registration	62

<i>Appendix B: Interpolation Algorithms</i>	63
B.6 Nearest Neighbor Interpolation	64
B.7 Linear Interpolation	65
B.8 Cubic Interpolation	66
<i>Appendix C: Nearest Neighbor Search Algorithms</i>	67
C.9 Exhaustive Search	68
C.10 Delauney Triangulation	69
C.11 K-D Trees	70
<i>Appendix D: Feature Detection Algorithms</i>	71
D.12 Harris Corner Detector	72
D.13 Shi & Tomasi's Minimum Eigenvalue Method	73
D.14 FAST Corner Detector	74
<i>References</i>	75

LIST OF TABLES

4.1 Alignment Results for Image Registration Methods	51
--	----

LIST OF FIGURES

1.1	Comparison Diagram of Dose Distributions of Proton Beam Therapy and X-Ray Radiation Therapy	7
3.1	Interpolation of Points on a Coarse Sine Curve	20
3.2	Phase Correlation of Unaltered and Shifted Versions of a Stock Image	23
3.3	Conditional Entropies $H(X Y)$, $H(Y X)$ and Mutual Information $I(X, Y)$ for Sets X and Y	25
3.4	2-D Delaunay Triangulation with Labeled Vertices and Triangles . . .	32
3.5	2-D K-D Tree of a Set of Points Along a Sine Curve	33
3.6	Diffeomorphic Registration of a Patient Lung	35
4.1	Input Reference and Captured 2-D Beamline and Orthogonal Images	38
4.2	Input Reference and Captured 2-D Beamline and Orthogonal Images Using FAST Corner Detector	40
4.3	Input Reference and Captured 2-D Beamline and Orthogonal Images Using Harris Corner Detector	41
4.4	Input Reference and Captured 2-D Beamline and Orthogonal Images Using Shi & Tomasi's Minimum Eigenvalue Method	43
4.5	Image Comparisons between Unregistered Images and Log-Polar Phase Correlation Output	45
4.6	Image Comparisons between Unregistered Images and Mutual Information Maximization Output	46

4.7	Image Comparisons between Unregistered Images and Enhanced Correlation Coefficient Maximization Output	47
4.8	Image Comparisons between Unregistered Images and Iterative Closest Point Output	48
4.9	Image Comparisons between Unregistered Images and Log-Domain Diffeomorphic Registration Output	50

1. INTRODUCTION

1.1 Overview

This thesis surveys various image registration algorithms to obtain an optimal, fiducial-free method for patient alignment during intracranial radiosurgery. Image registration is a widely-used technique to map a given image to a separate reference image in order to estimate the optimal transformation between them. Typically, the procedure for manual patient alignment at LLUMC includes digitally reconstructed radiographs (DRRs) of a computed tomography (CT) scan conducted during the treatment planning phase that act as the reference images, while digital x-ray images captured in the treatment room act as the images to be aligned. For this research, these images were taken of a skull phantom and used to test the image registration algorithms. These images are stored in the DICOM file format, a standard for handling information in medical imaging, and processed using the MATLAB numerical computing environment. This thesis analyzes several algorithms for image registration, including an extended phase correlation technique using log-polar coordinates [30], a mutual information maximization method [24, 29], an enhanced correlation coefficient (ECC) maximization method [12], various iterative closest point (ICP) methods [6, 18], a log-domain diffeomorphic registration method [37], and partial differential equation (PDE)-based methods [39, 38]. These registration methods were tested against beam-

line and orthogonal orientations of the skull phantom for accuracy, robustness, and performance. Shifts of no greater than 0.5 mm and rotations of no greater than 0.5° of the expected results were desirable, although slightly less precise results were also noted for further optimization. Scaling and shear are not factors for the duration of the radiosurgery procedure and were thus not considered in this research. Each algorithm was expected to run no longer than an maximum time of 300 seconds, the estimated minimum time required for manual alignment.

1.2 Background

An important aspect of effectively treating a patient with beams of radiation is that the patient be aligned as accurately as possible to prevent damage to healthy tissue. Current methods for intracranial radiosurgery at LLUMC utilize titanium fiducial markers implanted into the patient's skull to assist with the alignment of the patient [20]. Implanting these fiducials requires the patient to undergo a pre-treatment surgery which adds an element of physical and emotional stress and delays the overall treatment due to the additional scheduling, surgery, and healing. The healing process for this surgery alone may last between two to four weeks.

After the patient has recovered from surgery, a CT scan is conducted to identify the size and location of the tumor and to produce the reference DRRs for use during alignment verification. During treatment, the patient is physically immobilized while the therapist/physician aligns the patient using two orthogonal x-ray images against the reference DRRs. The therapist/physician uses the fiducial markers and/or bony landmarks to mark alignment points on the digital x-ray and reference images of the

patient's skull. An alignment algorithm calculates the correction translations and rotations which are then performed to align the anatomical target to the proton beam isocenter, the intersection of the beam axis with the gantry rotation axis. This step is repeated to assert accurate alignment until treatment has concluded. Manual alignment poses issues with efficiency, allows for human error, and requires personnel who are specifically trained in patient alignment. Alignment for each beam costs between five to eight minutes, with an average case of three to four beams per treatment, resulting in a total estimated time of fifteen to thirty-two minutes.

1.2.1 Introduction to Stereotactic Radiosurgery

In 1951, Swedish neurosurgeon Lars Leksell defined radiosurgery as “a single high dose fraction of radiation, stereotactically directed to an intracranial region of interest” [19]. Radiosurgery operates by concentrating beams of ionizing radiation from multiple directions at intra- and extracranial tumors and other lesions. The beams converge inside the target volume, delivering a greater dose of radiation to the intended area while leaving the surrounding healthy tissue exposed to lower levels of radiation. This lethal dose of radiation damages the DNA of the tumor cells, effectively killing their ability to reproduce. Benefits over traditional surgical procedures include the reduction of the risk of surgical complications and the elimination of potential side effects of general anesthesia. Typically, radiosurgery treatment is administered over a single session and does not require a hospital stay. Three modalities of stereotactic radiosurgery exist: the Gamma Knife, linear accelerator based therapies, and proton beam therapy. The focus of this research is for use with proton beam

therapy; however, image registration can be applied to all forms of patient alignment.

1.2.2 Gamma Knife

The Gamma Knife is a product of Elekta AB, a company founded by Leksell. This system was first implemented as a 179 source Cobalt-60 Gamma Knife prototype. Built in 1968 at the Sophia Hemmet Hospital in Stockholm, Sweden, this device was designed by Leksell and an associate by the name of Borje Larsson. Modern Gamma Knife therapies use a 201 source model, the first of which was installed at the University of Pittsburgh in 1987 under the direction of Dade Lunsford.

Contrary to what its name implies, the Gamma Knife does not require the use of a blade. Instead, it uses Cobalt-60, a radioactive isotope of cobalt, as a source of gamma radiation to treat tumors and other lesions in the brain without requiring any incisions or openings in the patient's skull. The Gamma Knife is primarily used to treat brain tumors, arteriovenous malformations (AVMs), trigeminal neuralgia, acoustic neuroma, and other functional problems.

Prior to treatment, a frame used to hold a specialized helmet is surgically attached to the patient's skull. The location of the tumor is then identified using a medical imaging procedure such as a CT scan, and a radiation therapy team determines the treatment plan based on this procedure. To maintain alignment of the beams, the patient is positioned and the specialized helmet is placed over the frame. This helmet acts as guide to focus the beams to the designated target. Treatment for the Gamma Knife may last between a few minutes to a few hours.

1.2.3 Linear Accelerator Systems

The first linear accelerator (LINAC) designed for medical purposes was an 8 MeV cyclotron built in 1952 at the Hammersmith Hospital in London [7]. This machine treated its first patient in 1953 and was in use for medical treatment until 1969. The first patient in the US to be treated by this type of radiation therapy was a two-year old boy with retinoblastoma. This treatment was conducted by Dr. Henry Kaplan at the Stanford University Hospital in 1956.

LINAC systems use high-energy x-rays that can treat large tumors, extracranial lesions, as well as areas other than the brain. These systems can generally treat larger volumes than Gamma Knife systems because LINACs use a gantry that has the ability to rotate around the patient during treatment. LINACs use electron beams to treat patients, which also differs greatly from Gamma Knife systems as it does not use radioactive materials as a radiation source. Instead, the x-rays are produced from the collision between the accelerated electrons and heavy metal targets. A collimator is used to shape the x-rays to the volume of the target.

The procedure for LINAC systems begins with a simulation. The tumor is located using a CT scan or other medical imaging machine, and the radiation team determines the best treatment plan for the patient. During treatment, the patient is situated on a mobile platform and positioned using lasers. Other tools can be used to assist in patient alignment, such as a face mask or alignment marker tattooed onto the patient's skin. More recently, however, these external tools are being replaced with image-based systems using 2-D radiographs or volumetric imaging such as cone beam CT.

1.2.4 Proton Beam Therapy

Robert R. Wilson, an American physicist, suggested the use of protons as an effective radiological treatment [40]. Protons were first used for treatment of a patient at the Berkeley Radiation Laboratory in 1954 and on several other occasions in the years that followed. However, the first hospital-based proton beam clinic was not operational until 1990, when the Fermi National Accelerator Laboratory (Fermilab) completed the construction of a 250 MeV proton synchrotron for Loma Linda University in Loma Linda, California [16, 25]. Currently, there exist approximately 34 clinical proton radiotherapy facilities worldwide.

Proton beam therapy is a charged-particle radiotherapy treatment that can be used for radiosurgical applications and provides several benefits over treatments that utilize gamma rays or x-rays. Charged particles can be more finely controlled and have no exit dose due to how the energy is released. This form of radiosurgery allows for a highly precise radiation dose distribution, which is especially advantageous for treating irregularly-shaped tumors, lesions bordering critical structures, and children due to their higher susceptibility to intellectual disorders and other potential side-effects caused by ionizing radiation [21]. According to recent publications [20], more than 15,000 neurosurgical patients and 12,000 ocular patients have been treated with charged-particle radiosurgery.

Protons are positively charged particles that exhibit behavior different from x-rays in that they penetrate matter only to a limited depth. As the protons slow down, they interact with more surrounding particles and thus a larger dose of energy is deposited into the tissue until the protons stop and all their energy has been released. The dose

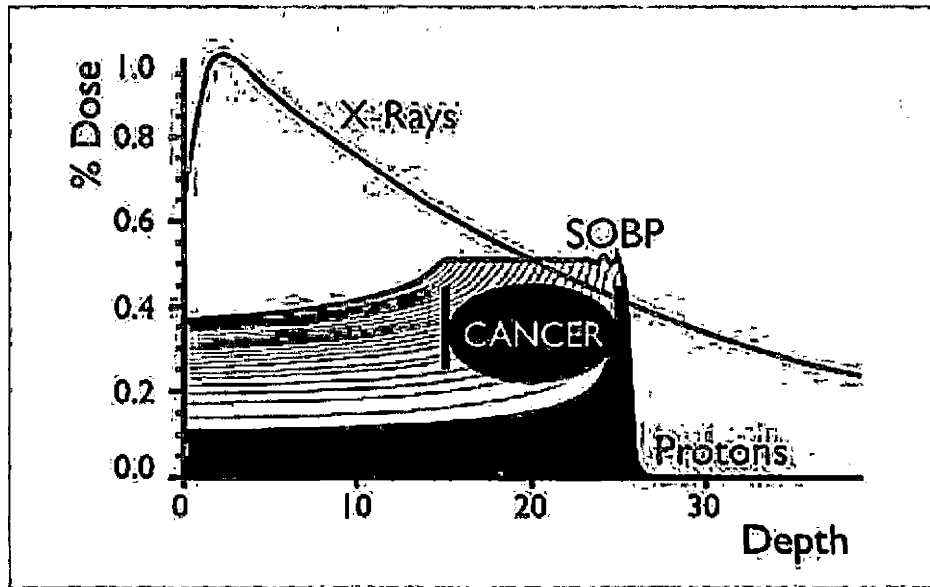


Fig. 1.1: Comparison Diagram of Dose Distributions of Proton Beam Therapy and X-Ray Radiation Therapy [10]

distribution can be modeled by a graph called the Bragg curve, where the maximum energy released is a sharp peak called the Bragg peak, named after its discoverer Williams Henry Bragg in 1903. The entry dose is relatively low, so the healthy tissue is exposed to a low level of radiation, until the beam enters to the targeted mass. To accommodate the size of the tumor, a modulator is used to spread the bragg peak to the full depth of the tumor. Figure 1.1 shows the comparison of dose distributions of the modulated Bragg Peak and standard x-rays, where the purple lines indicate the spread out Bragg peak (SOBP) as a cumulation of the unmodulated Bragg peaks, and the red line indicates the x-ray photon beam. The proton comes to rest immediately after the Bragg Peak occurs, leaving little to no exit dose of radiation.

1.3 Purpose

This thesis serves as both a proposal to adopt image registration a semi-automated, fiducial-free method for patient alignment verification during intracranial radiosurgery and a survey of registration algorithms for their capabilities for this purpose. An alignment system using image registration would provide significant improvements over current methods including the elimination of the dependency on the fiducial markers and the reduction of time the patient spends in the treatment room. Without the fiducials, the patient no longer requires the additional surgery for implantation which significantly shortens the acceptance time before treatment. Other benefits include the avoidance of infection, minimization of growth of the cancerous tissue, and reduction of the time before the physician can provide care for the patient. Without these delays in treatment planning, the overall treatment process can be reduced from about a month to approximately a week.

Similar research efforts have shown image registration as a plausible technique for patient alignment during radiosurgery procedures. Some examples of similar research include external video tracking using non-rigid feature-based registration [4], mutual information similarity metrics [3], and pattern matching methods using fiducials as alignment guides for registration [17]. This thesis seeks to expand upon this research to find the optimal methods for patient alignment for intracranial radiosurgery to implement in an actual hospital setting.

1.4 Scope

Two-dimensional (2-D) imaging is common practice for patient alignment during radiosurgery and radiotherapy procedures. As this is the standard methodology, this thesis focuses on 2-D image registration methods using the resources already used for manual alignment at LLUMC, which adds the benefit of applying to most treatment centers. While 3-D imaging or real-time systems are viable for future research, it is still in its infancy and as it develops so will volumetric alignment techniques. 2-D methods are examined here due to the time and costs of implementing new hardware and software systems and its proven track record. By using the reference and captured images from the current process, patient alignment can be automated without additional hardware costs and would only require a relatively minor development effort.

The registration algorithms are tested using reference and captured images currently used for patient alignment at LLUMC. The reference and captured images are acquired using different machines, so the algorithms analyzed are limited by multimodality registration requirements to account for the differences between these image capturing methods.

1.5 Definition of Terms and Abbreviations

Technical terms and abbreviations as applied to this thesis are defined in this section for the reader's convenience.

2-D 2-Dimensional space is a geometric model of the flat surface region of the images

taken from the various medical imaging modalities used for this research. This space is represented as width and height.

3-D 3-Dimensional space is a geometric model of the physical universe. In medical imaging, this space is typically represented as width, height, and depth.

Algorithm A sequential procedure used for calculation, data processing, and/or automated reasoning.

Beamline (image orientation) Beamline refers to the line along which the radiation beam travels. The beamline orientation is the image of the face of the skull.

Big O notation Big O notation is used to classify algorithms by the growth rate of their processing time or space requirements based on changes to input size.

Bragg Peak The Bragg peak denotes the sharp rise on the Bragg curve which plots the radiation dose as the particles travel through matter.

Cobalt-60 Cobalt-60 is a synthetic radioactive isotope of cobalt with a half-life of 5.27 years.

CT Computed Tomography is a medical imaging procedure that uses x-rays to produce cross-sectional images of specific areas of the body. "Tomography" stems from the Greek words "tomos," meaning section or slice, and "graphe," meaning drawing.

DRR A Digitally Reconstructed Radiograph is a 2-D simulated image rendered from a CT scan.

DICOM Digital Imaging and COmmunications in Medicine is a standard in medical imaging that has many uses; however, for the purposes of this thesis it is only used as a file format definition for storing 2-D CT and x-ray image data.

ECC Enhanced Correlation Coefficient is a modified version of the correlation coefficient used to measure the linear dependence between two variables, the reference and captured images to be aligned as applied to this thesis. These modifications grant sub-pixel accuracy and additional robustness in the presence of photometric distortions.

FAST Features from Accelerated Segment Test is a corner detection method used to extract the feature points in an image.

FFT The Fast Fourier Transform is an algorithm for converting a function of time or space to a function of frequency, or the number of occurrences of an event within a specified interval of time.

Fiducial marker An object placed in the field of view of an imaging system which appears in the images produced. In reference to this thesis, this is a surgical screw that is implanted into the patient's skull and used for patient alignment during intracranial radiosurgery.

Gamma Knife The Gamma Knife is a radiosurgical treatment that uses Cobalt-60 isotopes as its radiation source.

ICP Iterative Closest Point is an algorithm in image processing used to minimize the difference between two sets of points.

Image noise Image noise is the random variation of brightness or color in an image produced by the sensor used to capture the image.

LINAC LINear ACcelerator systems use external beam radiation to treat patients afflicted with cancer. These systems focus high-energy x-rays to the tumor volume to damage the cancerous tissue while minimizing harm to the surrounding healthy tissue.

LLUMC Loma Linda University Medical Center is a teaching hospital on the Loma Linda University campus located in Loma Linda, California, United States. This research was conducted under the clinical supervision of Dr. Andrew Wroe and Dr. Reinhard Schulte, faculty members of the department of radiation medicine at this institute.

MATLAB MATrix LABoratory is a numerical computing environment and programming language that specializes in matrix manipulations, plotting of functions and data, and implementation of numerical algorithms.

Orthogonal (image orientation) An orthogonal image with respect to the orientation of a patient's skull is of the left side of the skull, i.e. the face of the skull is directed toward the left side of the image.

PDE A Partial Differential Equation is a mathematical equation used to solve problems involving unknown functions of multiple independent variables and the partial derivatives of the unknown function with respect to those variables.

Proton beam therapy Proton beam therapy is a form of charged-particle radiotherapy that uses protons, instead of gamma rays or x-rays, to treat patients due to ease

of control and lack of an exit dose of radiation.

RANSAC The **R**ANdom **S**Ample Consensus algorithm is an iterative method to estimate parameters of a mathematical model in the presence of a large quantity of outliers.

Stereotactic Radiosurgery Stereotactic radiosurgery is a form of radiation therapy that delivers highly focused beams of radiation from multiple directions to a precise region of interest, such as a tumor or other lesion, located within the patient's body. "Stereotactic" stems from the Greek words "stereo," meaning solid, and "taxis," meaning arrangement or order.

2. REVIEW OF THE LITERATURE

2.1 *Introduction to Image Registration*

Image registration is the process of estimating the optimal transformation that relates two sets of data. Data used in registration may include images captured from different sensors, at different times, at different depths, and from different perspectives [9]. This process has several applications in computer vision, medical imaging, target recognition, and satellite data analyzation.

Image registration algorithms can either operate in the spatial domain, which rely on intensity patterns or features in the images to be registered [6, 9, 12, 18, 22, 23, 24, 27, 29, 36, 37], or in the frequency domain which rely on properties of the Fourier transform for rigid transformations such as translation, rotation, and scaling [9, 23, 30]. Feature-based measures can rely on automatically generated point clouds of the images or from manually selected control points. The random sample consensus (RANSAC) algorithm [13] is designed for robust fitting of models where many data outliers are available, which would be of use to estimate the parameters of a transformation type between the images. Methods that operate in the frequency domain are not limited by noise or other artifacts usually present in medical images. The phase correlation algorithm makes use of the Fourier transform to find the relative translation from the peak of the correlation as well as rotation and scale after

converting the images to the log-polar coordinate system.

Image registration algorithms that operate in the spatial domain can be classified into either intensity-based [9, 12, 22, 23, 24, 27, 29, 36, 37] or feature-based [6, 9, 18, 23] methods. The images in the algorithms that operate in this domain have two distinct roles. One image functions as the reference image to be registered against while the other image functions as the target image, called the captured image when referring to the medical images used for patient alignment, to be registered to the reference image. Some algorithms may also refer to these images by other names as well, though the idea is the same. To register these images, the captured image is aligned with the reference image, meaning the algorithm finds the transformation values such as translation and rotation that transforms the captured image back to reference image. Intensity-based algorithms compare intensity patterns in images using correlation metrics such as mutual information or correlation coefficient maximization thereby registering the entire images or subsections of the images, while feature-based methods find correspondence between features present in both images such as edges and corners thereby registering the images based on a point-by-point mapping of the images.

Image registration algorithms also operate based on specific transformation models that relate the two images. These models are essentially either based on linear transformations [9, 12, 18, 22, 23, 27, 29, 30] or non-rigid transformations [6, 9, 23, 24, 36, 37]. Linear transformations include translation, rotation, scaling, and other affine transformations, while non-rigid transformations warp sections of the captured image to align it with the reference image. This thesis primarily focuses on algorithms that operate on linear transformations because the patient can not be warped

for treatment.

Image registration algorithms also differ by modality of the sensors used to obtain the images. Single modal methods register images captured by the same sensor type, such as using the same camera to acquire the reference and target images. Multi-modal methods register images captured by different sensor types, which is more typical of medical imaging [23], such as registration of brain CT/MRI images. This thesis focuses on multi-modality methods since the reference images are taken from a CT scan and the captured images are taken in the treatment room.

Image registration algorithms can provide certain levels of automation. For example, manual methods merely provide the tools for alignment but must rely on the user to perform and verify the actual alignment. Interactive methods are more automated, but still require a user to guide the registration. Semi-automatic methods automatically align the images, but require the user to verify correctness of the alignment. Automatic methods are completely automated and do not allow for any user interaction. During comparison testing, the algorithms were completely automated to obtain the transformation results; however, these techniques may be used in several levels of automation. The manual system will remain in place at LLUMC to allow for verification of the image registration results, therefore the goal is to implement a semi-automated system.

2.2 Image Registration in Medical Imaging

Fiducial markers are a common tool used in registration for medical imaging. These opaque markers are placed on or inside the patient to provide a frame of reference

between image sets. The purpose of these fiducials is to create a visible reference used to verify comparisons made between two or more images, typically captured from different modalities. As an example, these fiducials are typically used during multi-modal image registration for mapping single-photon emission computed tomography (SPECT) or positron emission tomography (PET) data to anatomical information from magnetic resonance imaging (MRI). A comprehensive overview of the categories of image registration and their applications is shown in [23].

3. METHODS FOR IMAGE REGISTRATION

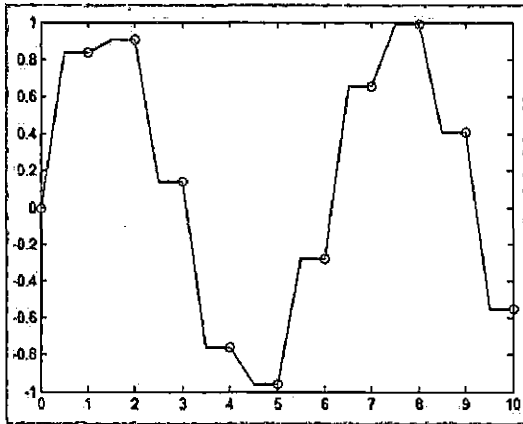
3.1 *Introduction*

This thesis investigates several methods for image registration for their capability to provide an optimal alignment within a reasonable duration of time over current manual alignment methods. While the intent of this thesis is to provide a sufficient selection of algorithms for testing, certain categories of algorithms are more obvious for the purpose of this research. For example, as different sensors are used to capture the reference and captured images, multi-modal algorithms are required. The registration algorithms must also account for the entire image as a single transformation from the captured image to the reference image in order to obtain the transformation information that will be used to verify the alignment of the patient. The following sections describe the image registration algorithms considered for this research. Each algorithm was implemented using the MATLAB computing environment. Several tools are readily available within this environment, including methods for interpolation, nearest neighbor search, and even the mutual information maximization image registration algorithm compared in this thesis. A basic pseudocode implementation for each algorithm is also provided in the appendix.

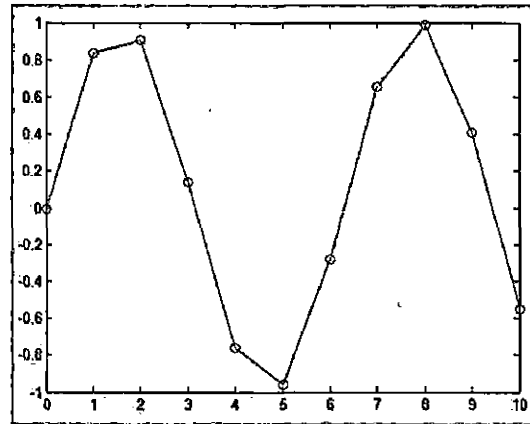
3.2 Interpolation

In image processing, it is necessary to construct new data points around already known points for image transformations such as rotation or resizing. This method is called interpolation [1]. Several algorithms presented in this thesis implement interpolation for various purposes, so it is presented in its own section here. The three primary methods for interpolation for use with image processing are nearest neighbor, bilinear, and bicubic interpolation. Figure 3.1 shows a number of graphs of a set of data points along a sine curve. Each graph of the set shows a different interpolation implementation used to construct a line connecting the points in the set.

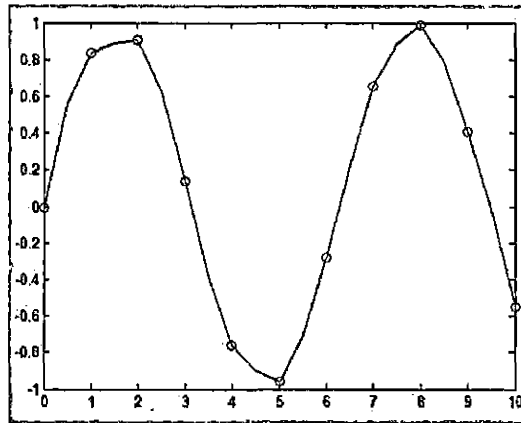
In nearest neighbor interpolation, the value of the nearest point is selected which results in a piecewise constant function. This algorithm is easy to implement and commonly used in texture filtering. Bilinear interpolation simply extends linear interpolation by interpolating in two dimensions. This method of interpolation uses linear polynomials to construct a curve to best fit a series of data points. In image resampling, bilinear interpolation uses four surrounding pixels to estimate the value of an unknown pixel. Bicubic interpolation also extends its counterpart, cubic interpolation, by interpolating in two dimensions. Bicubic interpolation provides smoother surfaces than those provided by bilinear and nearest neighbor interpolation, and is typically used in image resampling when performance is a low priority. Sixteen surrounding pixels are used to estimate the value of the unknown pixel. Lagrange polynomials, cubic splines, and cubic convolution are all algorithms that can be used to perform bicubic interpolation.



(a) Nearest Neighbor Interpolation



(b) Linear Interpolation



(c) Cubic Interpolation

Fig. 3.1: Interpolation of Points on a Coarse Sine Curve

3.3 Phase Correlation Using Log-Polar Coordinates

Image registration can be performed in the frequency domain to take advantage of several properties of the Fourier transform for simple transformations. The peak of the phase correlation between the reference and captured images is the translational difference between the two images. The approach chosen for this thesis extends the phase correlation technique by converting the images from Cartesian coordinates to log-polar coordinates in order to also obtain the rotational difference [30]. The Cartesian coordinate system in two dimensions is a rectangular coordinate system stemming from two perpendicular lines typically known as the x and y axes. Every point on this plane is given a value for its x and y locations. In imaging, the labels for the x and y axes are usually the width and height of the image. The log-polar coordinate system is also denoted by two values: the logarithm of the distance from the point to the origin (i.e. the point at $(0,0)$) and the angle from the line between the point and the origin and the line designated as the x -axis. For this algorithm, bilinear interpolation is used to convert between the coordinate systems.

This algorithm begins by calculating the fast Fourier transforms (FFTs) of the reference and captured images.

$$F_a = \mathcal{F}(f_a)$$

$$F_b = \mathcal{F}(f_b)$$

Multiplying the FFT of the reference image and the complex conjugate of the FFT of the captured image by each element and normalizing by each element will produce

the cross-power spectrum of these images.

$$R = \frac{F_a \circ F_b^*}{\|F_a F_b^*\|}$$

Taking the inverse FFT of this and finding its peak produces the relative shift between the images.

$$r = \mathcal{F}^{-1}(R)$$

$$(\Delta x, \Delta y) = \text{max}(r)$$

Performing this technique after converting to log-polar coordinates will produce the rotation. An example is shown in figure 3.2, where the phase correlation produces a third matrix with each element empty except at the peak. This is known as an impulse function. The order in which the translation and rotation is performed is interchangeable, which allows this algorithm to be parallelized for further performance improvements.

As it produces fewer artifacts than other methods, the phase correlation technique is commonly used in frame rate conversion [8]. The advantage of this method over other algorithms used for frame rate conversation is its ability to find motion within a block allowing for finer conversion than simply matching a given block between frames. The peak of the phase correlation estimates possible motion within that block. This allows for the direction and speed to be directly measured rather than estimating and extrapolating, producing better accuracy and thus less artifacts.

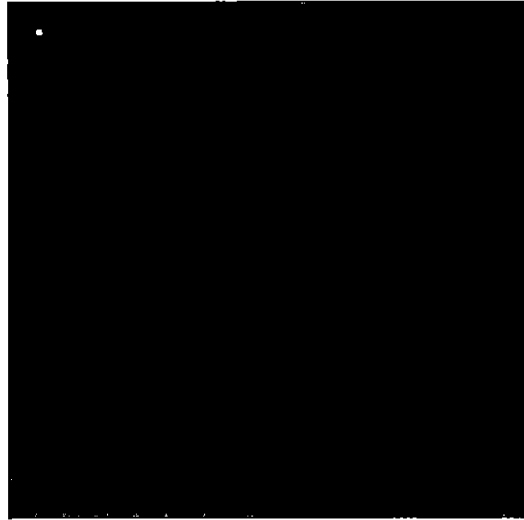
As this is not an iterative algorithm, the phase correlation technique is computa-



(a) Unaltered stock image



(b) Shifted stock image



(c) Phase correlation of stock image

Fig. 3.2: Phase correlation of Unaltered and Shifted Versions of a Stock Image [35]

tionally efficient. This algorithm is also highly resilient to noise and allows rotation to be found invariant to translation, which allows for both transformations to be computed simultaneously and/or in either order.

A disadvantage to this method is that performance is reduced if the shift is linear, as opposed to circular. A circular shift essentially wraps the portion of an image that would be shifted out of the original boundaries of the image to its opposing region of the image. For example, given a downward shift of ten pixels, the bottom ten pixels of the shifted image would be 'circle' around to the top of the image.

3.4 Mutual Information Maximization

Mutual information is a metric derived from probabilistic measures of image intensity values [24, 29]. This algorithm uses the joint probability distribution of the reference and captured images to iteratively measure the certainty that the captured image maps to the reference image. Mathematically, mutual information is defined as:

$$I(X; Y) = \sum_{y \in Y} \sum_{x \in X} p(x, y) \log\left(\frac{p(x, y)}{p(x)p(y)}\right)$$

where $p(x, y)$ is the joint probability distribution function and $p(x)$ and $p(y)$ are the marginal probability distribution functions.

The probability distributions are based on marginal and joint histograms of the reference and captured images. Higher mutual information implies lower uncertainty, thus also implying the images are more likely to be aligned than during previous iterations. This algorithm uses a specified number of samples used to compute the probability density estimates and the number of bins used to compute the uncertainty.

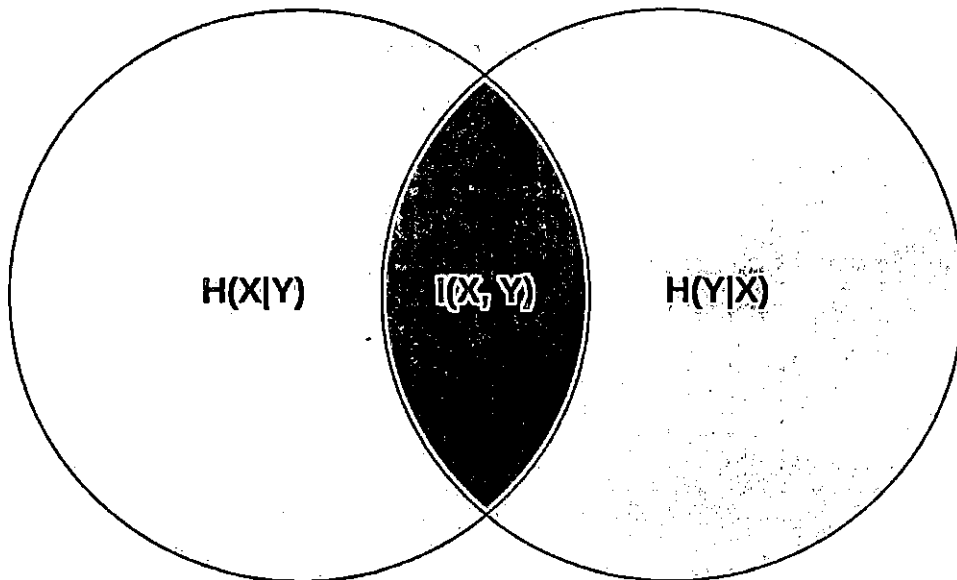


Fig. 3.3: Conditional Entropies $H(X|Y)$, $H(Y|X)$ and Mutual Information $I(X, Y)$ for Sets X and Y

The joint probability density function is then evaluated at each bin using the samples, while entropy is computed by summing over the bins. Zero- and third-order B-spline kernels are used to compute the probability density functions of both images. Figure 3.3 demonstrates the mutual information between two data sets.

Mutual information maximization is a direct measure of the probabilistic relationship of two random variables, which implies that if two images do not share mutual information, then they are not related by a particular transformation. This allows the algorithm to determine that two images cannot be aligned which can prove useful in some contexts.

As this is an iterative algorithm, it is inherently computationally intensive. Also, this algorithm can suffer in noisy conditions as the increase in noise results in a decrease in mutual information. Though this does not imply the images cannot be

aligned, finding an optimal alignment is more difficult.

3.5 Enhanced Correlation Coefficient Maximization

The enhanced coefficient correlation method [12] maximizes the linear dependence between the reference and captured images in order to achieve the optimal alignment. This algorithm uses an iterative forward additive approach, sacrificing computational efficiency for better accuracy. The difference from other algorithms using this metric, such as an inverse compositional approach, is that the forward additive approach uses an approximated parameter vector that is optimized each iteration until its norm becomes smaller than a pre-defined threshold set by the user.

The optimizing perturbation is defined as:

$$\Delta p = (\bar{G}^t \bar{G})^{-1} \bar{G}^t \left(\frac{|\hat{i}_c|^2 - \hat{i}_w^t P_G \hat{i}_c}{\hat{i}_r^t \hat{i}_c - \hat{i}_r^t P_G \hat{i}_c} \hat{i}_r - \hat{i}_w \right)$$

where G is the Jacobian matrix, \hat{i}_r and \hat{i}_c are the zero-mean normalized vectors of the reference and captured images, and $P_G = \bar{G}(\bar{G}^t \bar{G})\bar{G}^t$ is the orthogonal projection operator.

The enhanced correlation coefficient maximization algorithm begins with initializing a warping transformation matrix using a given initial estimate. Using the initial transformation estimate, the captured image is warped and the zero-mean vectors of both images are compared using the pre-defined threshold. This process repeats until the allotted amount of iterations and pyramid levels have been exhausted or the alignment has been determined optimal, whichever occurs first. This algorithm was chosen for this research as it has already been shown to be superior to similar algo-

gorithms such as the Lucas-Kanade [22] and simultaneous inverse compositional (SIC) [2] registration methods. While several versions of this method exist, for simplicity only the forward additive version was used for testing.

This algorithm is beneficial for this application as it is known for its robustness regarding noisy conditions and photometric distortions in contrast and brightness. However, this method has disadvantages that must be considered, including its computational complexity and that it does not imply causality. Uncorrelated variables may not necessarily be independent of each other, which means two uncorrelated images may still be related by a particular transformation that this method was unable to determine.

3.6 Iterative Closest Point Methods

The iterative closest point (ICP) method [6, 18] is an iterative, feature-based algorithm that essentially works in two steps. Each iteration first matches points based on the latest transformation estimate then refines the estimate based on the matches. This algorithm is simple to implement and allows the user to choose optimal sub-routines for feature detection and closest point calculation. Several corner detection algorithms were used for testing, including the Harris corner detector [15], the Shi and Tomasi minimum eigenvalue method [33], and the FAST corner detector [31, 32]. Multiple nearest neighbor search algorithms for finding the closest points between the images were also tested, but only the results for the K-D tree nearest neighbor search are shown in the results as it is the fastest of the three methods.

If the requirements of a good selection of points and initial transformation esti-

information are met, this algorithm is resilient when noise is present. Unfortunately, this algorithm is prone to accumulative errors as each iteration heavily relies on the calculated transformation of the previous iteration. This drawback explains the requirements of an accurate initial transformation estimate. Also, this algorithm requires the set of points for each image to correlate well with each other, which requires a good feature-detection algorithm for the images being used.

3.6.1 Feature Detection for Point Cloud Generation

Due to the nature of the ICP algorithm, the initial step for calculating the proper alignment between two images is to construct feature point clouds of both images. Several algorithms exist for finding features such as edges and corners within images, and, while not the focus of this thesis, a few of these algorithms are presented in this section.

Two similar corner detection algorithms are included in MATLAB and are used for testing point cloud generation for the reference and captured images. The default algorithm, the Harris corner detector [15], is a modification of the Moravec corner detector [26]. The Moravec detector determines the average change E in image intensity I from shifting a window within the image. The following rules apply and allow for the detection of the corners within an image:

1. If the window contains no features, then the average change in intensity will be small for shifts in all directions.
2. If the window contains an edge, then the average change in intensity will be small for a shift along the edge and large for a shift perpendicular to the edge.

3. If the window contains a corner, then the average change in intensity will be large for shifts in all directions.

While the Harris algorithm functions on the same principles, it seeks to improve upon a few shortcomings on the Moravec corner detector. The first of these issues is that the Moravec detector considers shifts at every 45 degrees. This behavior is enhanced in the Harris detector by considering all possible shifts about each point. The second of these issues is within the window w used by the algorithm. Moravec uses a binary, rectangular window, while Harris uses a circular window, also known as a Gaussian window. The last of these issues is the fact that the Moravec detector only takes into account the minimum change in intensity. The Harris detector improves upon this by using the variation of the change with the direction of the shift. This is shown in the following equations:

$$E(x, y) = \det(M) - k(\text{trace}(M))^2$$

$$\det(M) = \lambda_1 \lambda_2$$

$$\text{trace}(M) = \lambda_1 + \lambda_2$$

where

$$\begin{aligned}
M &= \begin{pmatrix} A & C \\ C & B \end{pmatrix} \\
A &= X^2 \otimes w \\
B &= Y^2 \otimes w \\
C &= (XY) \otimes w \\
X &= I \otimes (-1, 0, 1) \approx \left(\frac{\partial I}{\partial x} \right) \\
Y &= I \otimes (-1, 0, 1)^T \approx \left(\frac{\partial I}{\partial y} \right)
\end{aligned}$$

The Shi and Tomasi minimum eigenvalue method [33] is a further modified version of the Harris corner detector. The primary difference between the Harris corner detector and the Shi & Tomasi method is how the change in intensity is calculated, which is improved over the Harris detector. This is denoted by:

$$E = \min(\lambda_1, \lambda_2)$$

The third choice of algorithm for feature detection for point cloud generation is the FAST corner detector [31, 32]. This algorithm is characterized by its performance and repeatability. The repeatability of this algorithm is especially desirable due to the number of images taken of a single patient over a period of time. While the point cloud for the reference image is only generated once per treatment, each time alignment of the patient is verified a new point cloud would be generated based on a new captured image. Repeatability would ensure that the generated points would be of the same features across these images. This algorithm finds a corner by taking circles of 16 pixels and comparing the top, right, left, and bottom pixels on this circle

with the pixel at the center of the circle. For a corner to exist, at least three of these pixels must be brighter or darker than the center pixel.

3.6.2 Nearest Neighbor Search

Given two data sets, it may be useful to find the closest points between them in order to measure the similarity between the sets. In image registration, point clouds can be used to denote the various features within the images and can be used to find the optimal alignment between the images, as is done in the ICP algorithm. This can be accomplished by employing a method of nearest neighbor search.

A basic method for finding the closest points is to employ an exhaustive search, i.e. this naive algorithm calculates the distances between all points in both sets and choosing the ones with the shortest distances.

A more sophisticated approach is called a Delaunay triangulation [11]. A Delaunay triangulation for a set P of points in a plane is a triangulation $DT(P)$ such that no point in P is inside the circumcircle of any triangle in $DT(P)$. Figure 3.4 shows the Delaunay triangulation of a set of points on a 2-D graph.

A K-D tree (short for K-dimensional tree, where K denotes the number of dimensions of the tree) is a space-partitioning data structure for organizing points in a k-dimensional space [5, 14]. This structure is formulated by first taking the midpoint of a set of points and marks this point as the root. The points on either side of the root now form two subsets, which are recursively added to the tree by again taking their midpoints until all points have been added. Figure 3.5 shows a K-D tree of a set of points on a graph.

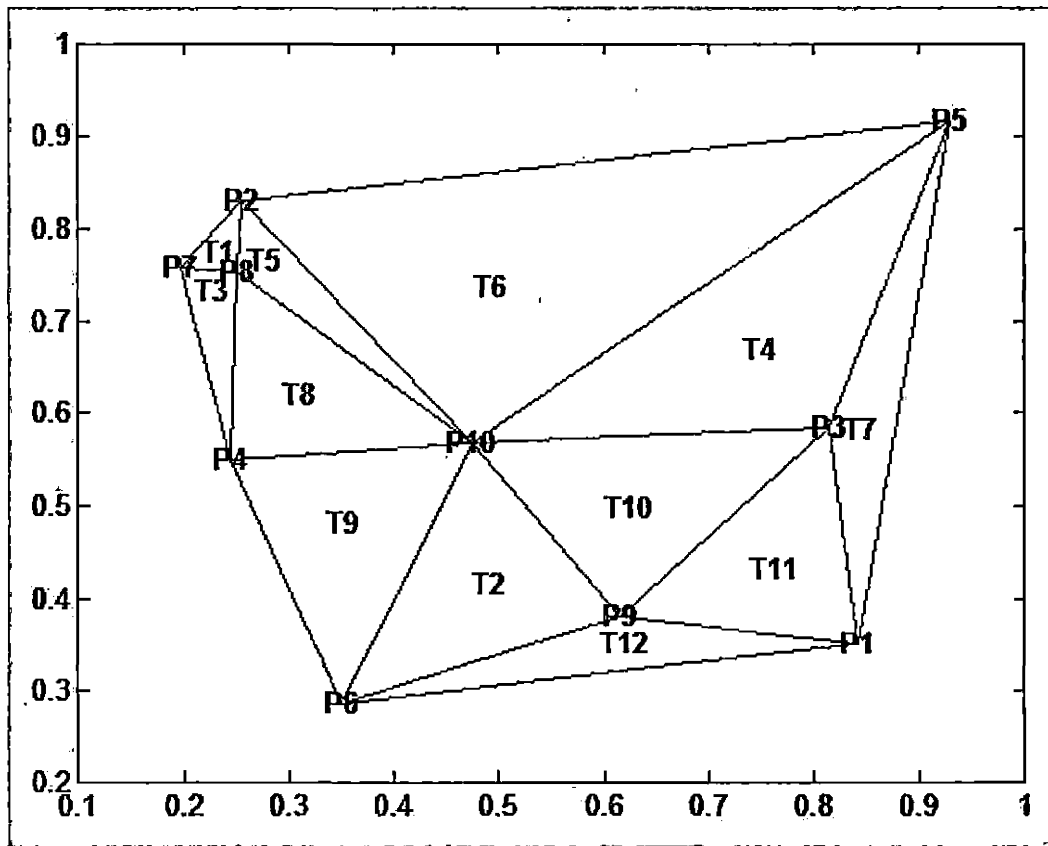


Fig. 3.4: 2-D Delaunay Triangulation with Labeled Vertices and Triangles

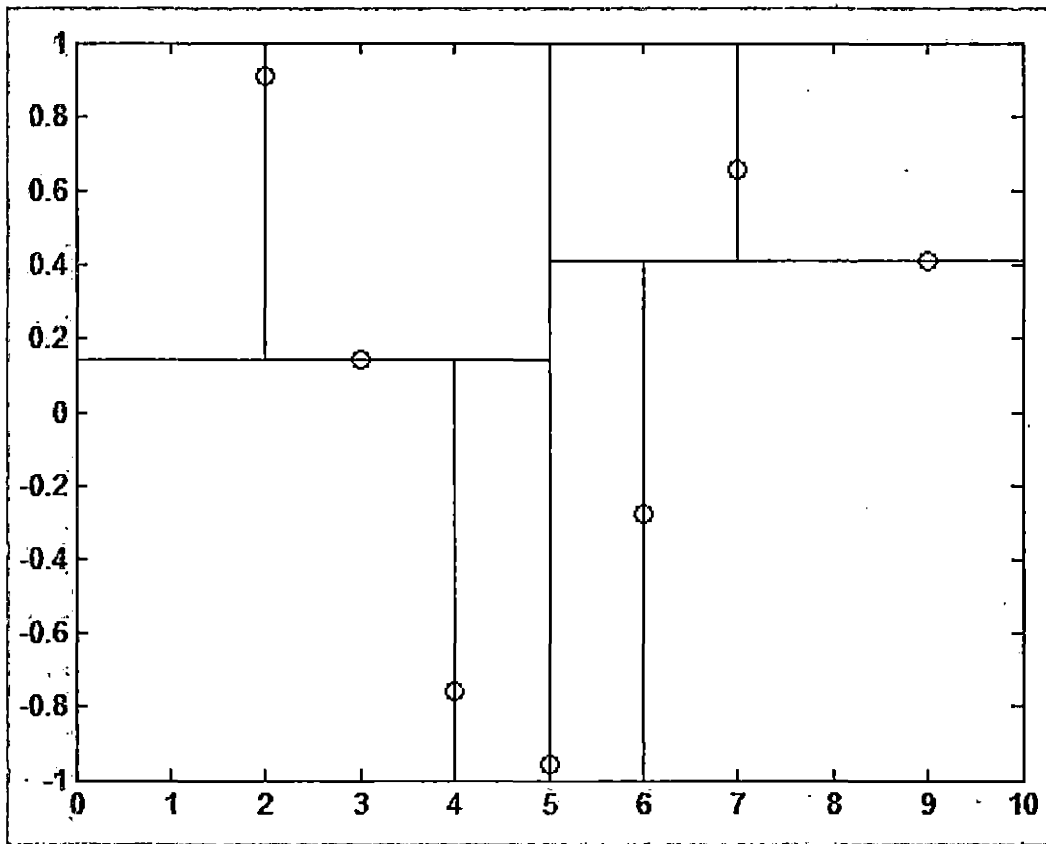


Fig. 3.5: 2-D K-D Tree of a Set of Points Along a Sine Curve

3.7 *Log-Domain Diffeomorphic Registration*

The log-domain diffeomorphic image registration algorithm [37] used in this research is a non-rigid registration algorithm that uses a stationary velocity field to register the reference and captured images. The algorithm represents the transformation of the current iteration as an exponential of the velocity field and then uses a modified version of Thirion's demons algorithm [36] to calculate the update field based on this transformation. Figure 3.6 shows the registration of a patient lung with respect to the same lung with deformities.

The demon algorithm began as a thought experiment by James Clerk Maxwell as a hypothetical violation of the second law of thermodynamics. In this experiment exists a container of gas molecules separated by an insulated wall with a door. This door can be opened and closed by what has come to be known as Maxwell's "demon," only to allow the faster molecules on one side and slower molecules on the other. One side of the container becomes hot and the other side becomes cold, resulting in a decrease in entropy.

The use of a velocity field allows for greater efficiency, however, an overall alignment estimate is not possible as it is not a linear transformation. For completion, however, the image output is displayed later in the results section.

3.8 *Partial Differential Equation-Based Methods*

PDEs are used in various computer vision and image processing applications, so they were briefly examined during this research for their potential application to image registration for medical imaging. PDEs are widely used for various applications in

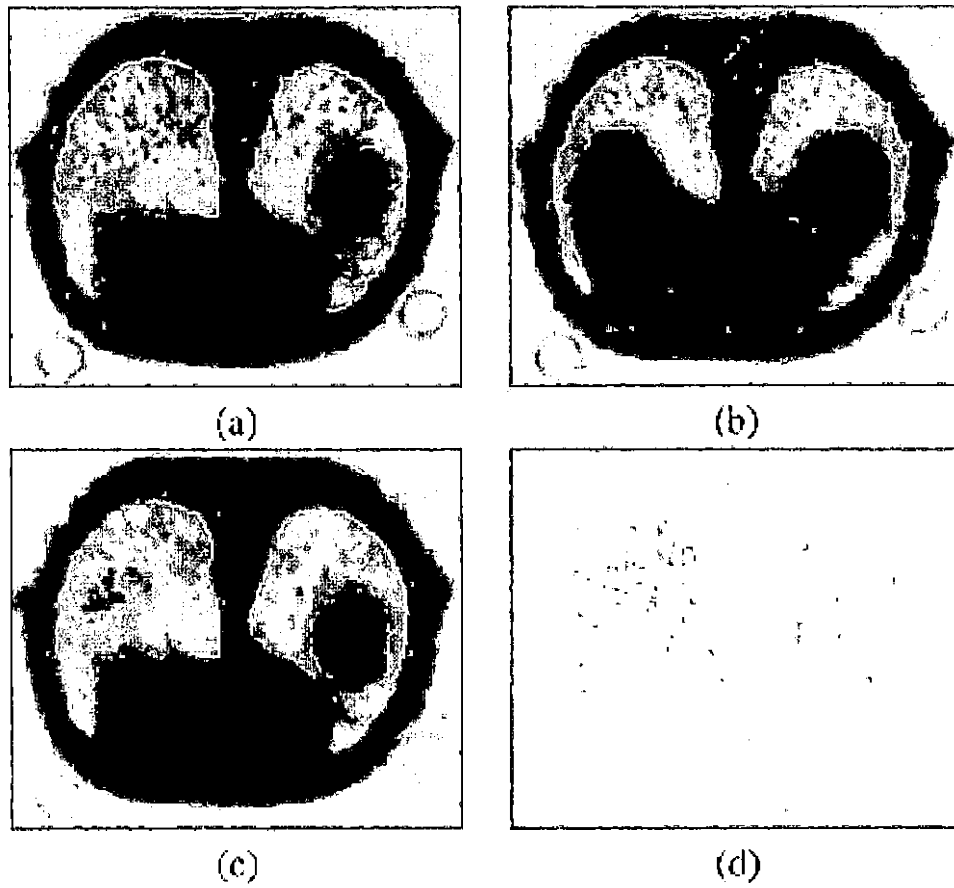


Fig. 3.6: Diffeomorphic Registration of a Patient Lung; (a) Original Patient Lung; (b) Deformed Patient Lung; (c) Demons Registration; (d) Difference between Images [27]

computer vision and image processing, even in medical imaging, such as anisotropic diffusion filtering [38] and image segmentation [39]. However, the benefits of PDEs to these applications did not seem to benefit this research and a PDE-based image registration algorithm was not implemented for testing. Their use for anisotropic filtering is more apt for textured images rather than the shape of a human skull, and segmentation methods would still require a separate alignment technique to calculate the relative transformation between the images.

4. RESULTS AND DISCUSSION

4.1 Introduction

Both the numerical transformation results as well as the visual representation of the alignments for each algorithm are presented in this chapter. A set of beamline and orthogonal images were used as input images for each algorithm. The images tested in this research are saved in the DICOM medical imaging format. The reference images are taken from a CT scan before treatment with a reported pixel size of $0.7999999821\text{mm} \times 0.7999999821\text{mm}$ and an approximate field of view of $409.59\text{mm} \times 409.59\text{mm}$ or $512\text{px} \times 512\text{px}$, while the captured images are DDRs taken in the treatment room during radiosurgery initially saved as a proprietary format (DI) and later converted to DICOM. The captured images have a reported pixel size of $0.268097\text{mm} \times 0.268097\text{mm}$ and a field of view of approximately $274.53\text{mm} \times 274.53\text{mm}$ or $1024\text{px} \times 1024\text{px}$. Due to the difference in scale, the captured images have been rescaled to fit the size of the reference images. Errors due to resampling may cause some slight issues on overall accuracy of the alignment, but the algorithms were not too impeded by this limitation. As the DICOM format is standardized, MATLAB contains built-in tools to process images saved in this format. First, the DICOM images are loaded into MATLAB as image matrices and separately as information objects for each image in order to use some of the image properties for checking scale between the images and

converting from a millimeter system to a pixel-based system.

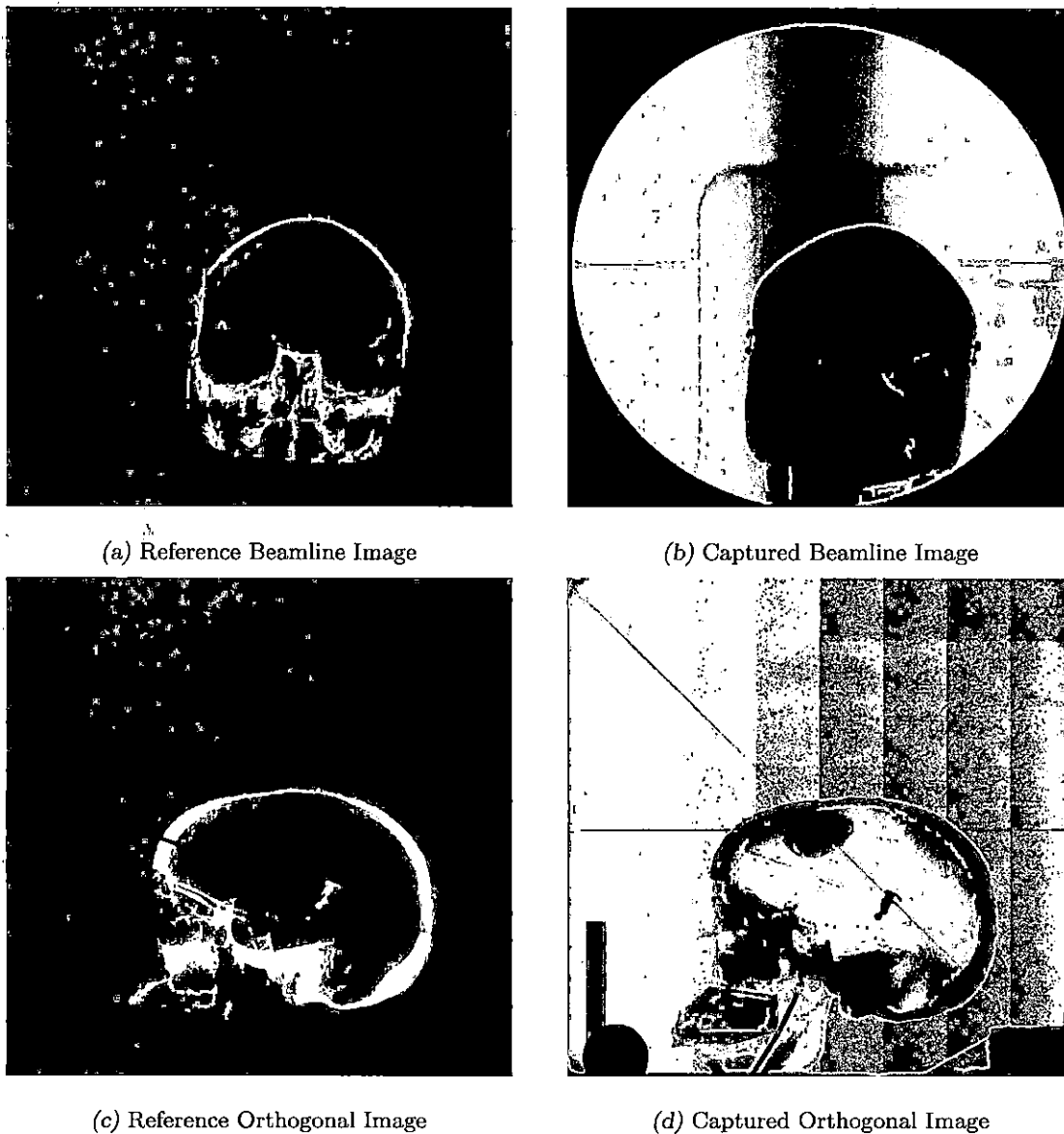


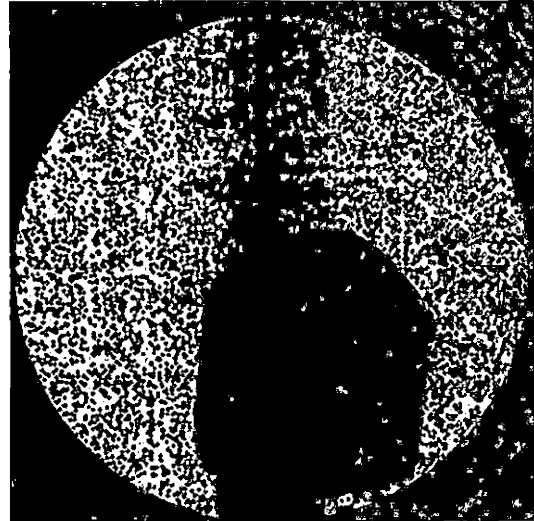
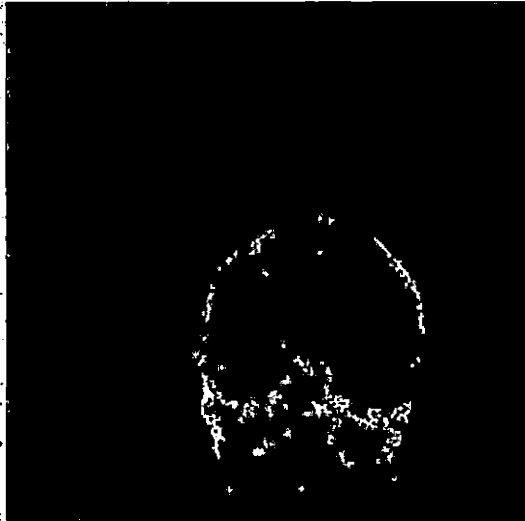
Fig. 4.1: Input Reference and Captured 2-D Beamline and Orthogonal Images

Figure 4.1 shows the 2-D beamline and orthogonal image sets used for testing the image registration algorithms. The subfigures to the left are the reference DDRs taken from a CT scan of a skull phantom, and the subfigures to the right are the captured 2-D x-ray images of the same skull phantom in the treatment room.

As an additional note, the iterative closest point registration algorithm requires two clouds of points that model the reference and captured images, and the results of the feature detection algorithms are also presented in this section in figures 4.2, 4.3, and 4.4. The red dots on these figures denote the detected corners by the respective feature detection algorithm. In executing the feature detection tests, the artifacts present on the images were discovered to cause complications while detecting the feature points, and as a result of these complications the two clouds of feature points did not have a sufficient mapping to allow for an optimal alignment. Noise is especially prevalent on the digital x-ray images taken during treatment and thus causes the most concern. This noise is caused by the difference in air scatter as opposed to in-patient scatter. X-ray photons are much less likely to scatter in the air, whereas there is a high likelihood they will scatter after penetrating tissue. When treating areas of the brain, the imaging area is much larger than the patient which causes the difference in scatter. This is called quantum mottle or quantum noise [34]. Noise can be reduced at the expense of patient exposure and dose, but exposing the patient to too much radiation can cause more undesirable issues.

Figure 4.2 shows the input images with the detected feature points using the FAST corner detector. For each point, this algorithm compares the intensity at that point with the intensities of each surrounding pixel in a circle. If three quarters of this circle have a lower intensity than that of the center pixel, a feature is found. Due to the random noise present in this image, this causes false detection of a large amount of points as features.

Figure 4.3 shows the input images with the detected feature points using the Harris

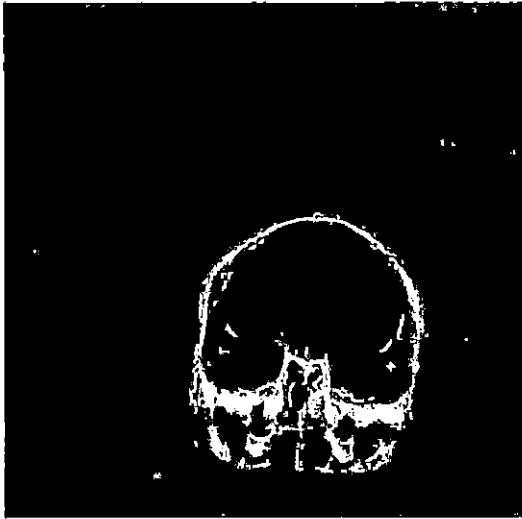


(a) Reference Beamline Image Using FAST Corner De- (b) Captured Beamline Image Using FAST Corner De-
tector tector



(c) Reference Orthogonal Image Using FAST Corner (d) Captured Orthogonal Image Using FAST Corner
Detector Detector

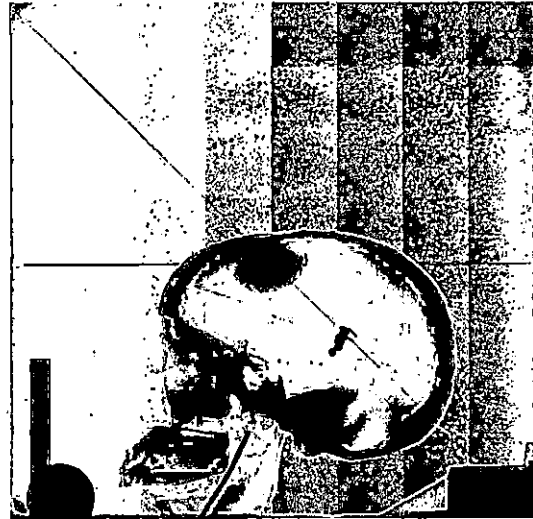
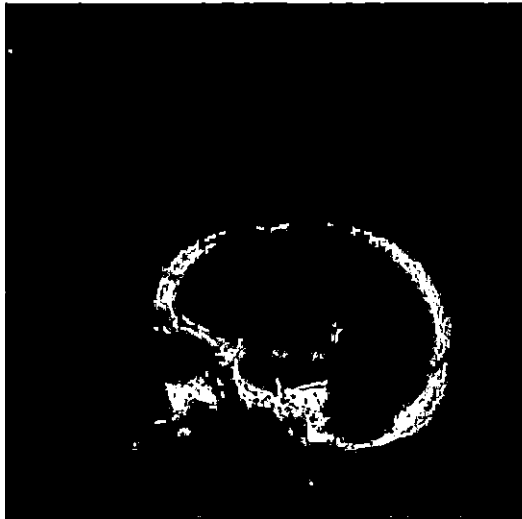
Fig. 4.2: Input Reference and Captured 2-D Beamline and Orthogonal Images Using FAST Corner Detector



(a) Reference Beamline Image Using Harris Corner (b) Captured Beamline Image Using Harris Corner

Detector

Detector



(c) Reference Orthogonal Image Using Harris Corner (d) Captured Orthogonal Image Using Harris Corner

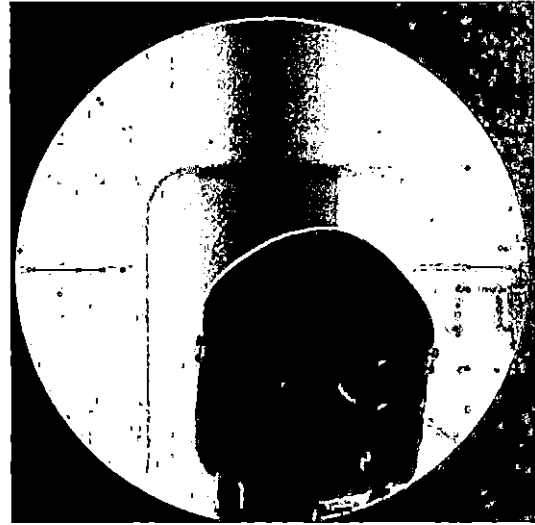
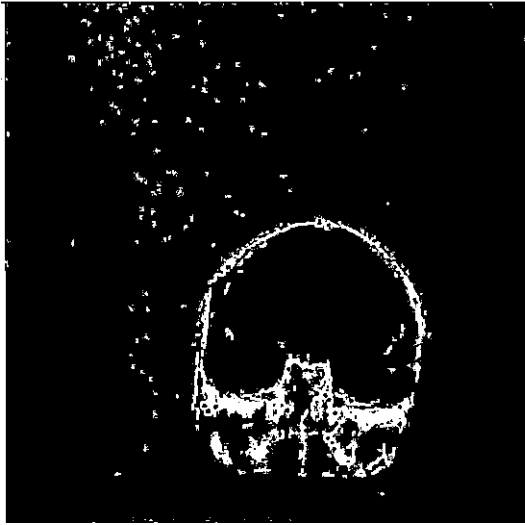
Detector

Detector

Fig. 4.3: Input Reference and Captured 2-D Beamline and Orthogonal Images Using Harris Corner Detector

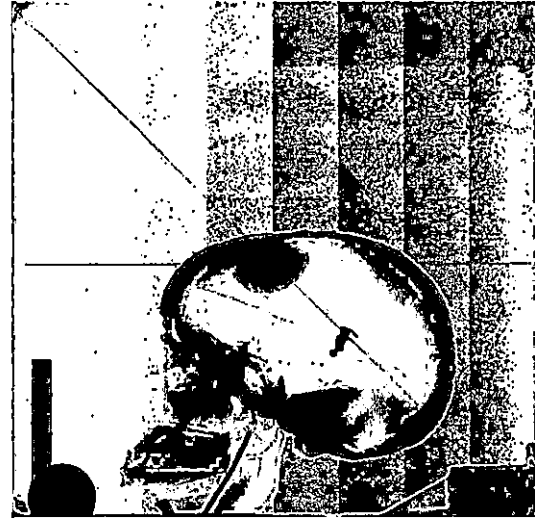
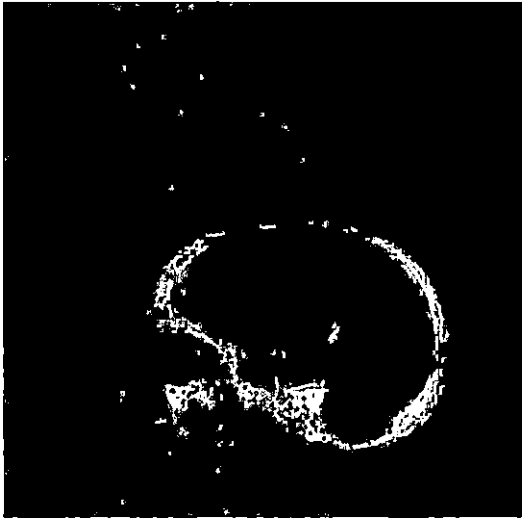
corner detector. This algorithm constructs a matrix using the partial derivatives of the input image and finds the features based on a score calculated by the determinant and the trace of this matrix.

Figure 4.3 shows the input images with the detected feature points using Shi & Tomasi's minimum eigenvalue method. This algorithm constructs the same matrix as in the Harris detector, but instead calculates the score using the minimum eigenvalues of the matrix.



(a) Reference Beamline Image Using Shi & Tomasi's
Minimum Eigenvalue Method

(b) Captured Beamline Image Using Shi & Tomasi's
Minimum Eigenvalue Method



(c) Reference Orthogonal Image Using Shi & Tomasi's
Minimum Eigenvalue Method

(d) Captured Orthogonal Image Using Shi & Tomasi's
Minimum Eigenvalue Method

Fig. 4.4: Input Reference and Captured 2-D Beamline and Orthogonal Images Using Shi & Tomasi's Minimum Eigenvalue Method

4.2 Comparison of Methods

This section contains the visual output of each registration method for the 2-D beamline and orthogonal images. The registered image sets are paired with their respective unregistered sets. Each set consists of the captured image overlaid atop the reference image. The reference and captured images are shown in an overlay fashion to visually demonstrate the accuracy of each algorithm. The green and magenta coloring scheme shows the difference between pixel values of the images, i.e. green denotes the difference of the reference image from the captured image while magenta denotes the difference of the captured image from the reference image.

Figure 4.5 shows the comparisons of the overlaid unregistered beamline and orthogonal images with their respective registered images using the phase correlation algorithm. These results show that the displacement after alignment between the registered images is very small, meaning that this algorithm appears to be highly accurate.

Figure 4.6 shows the comparisons of the unregistered images from the previous section with their respective registered images using the mutual information maximization method. This algorithm also appears to be visually accurate and thus a viable candidate for implementation.

Figure 4.7 displays the unregistered images with the registered images obtained from the ECC maximization method. Like the previous algorithms, this algorithm is also a good candidate for implementation for patient alignment.

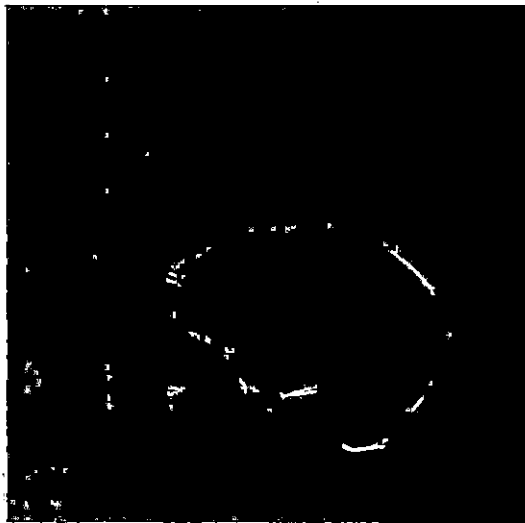
Figure 4.8 shows the unregistered images with the registered images obtained from the ICP algorithm. Complications arose with this algorithm due to the noise present



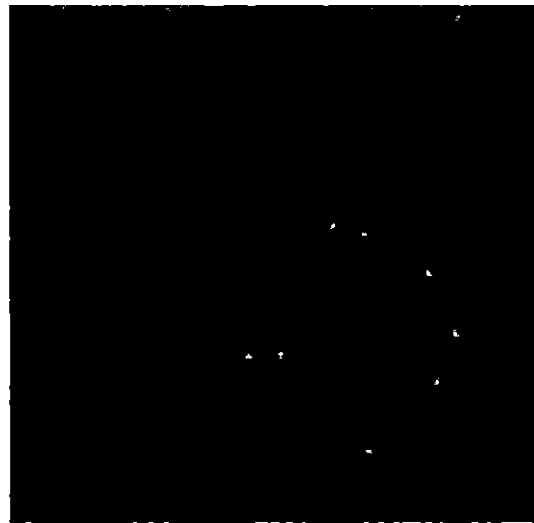
(a) Unregistered 2-D Beamline Images



(b) Registered 2-D Beamline Images

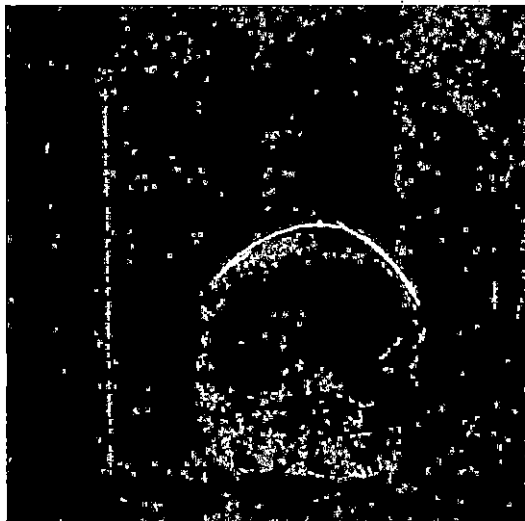


(c) Unregistered 2-D Orthogonal Images



(d) Registered 2-D Orthogonal Images

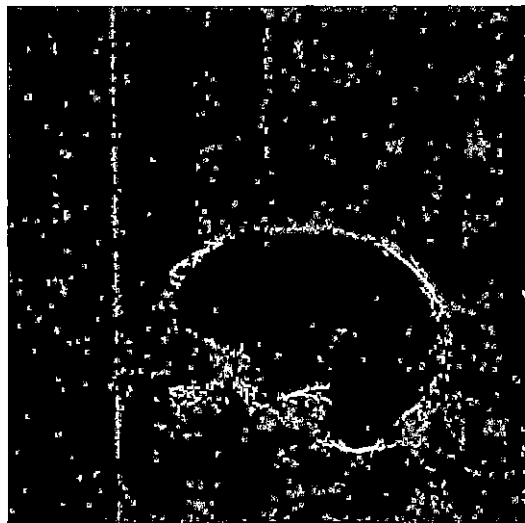
Fig. 4.5: Image Comparisons between Unregistered Images and Log-Polar Phase Correlation Output



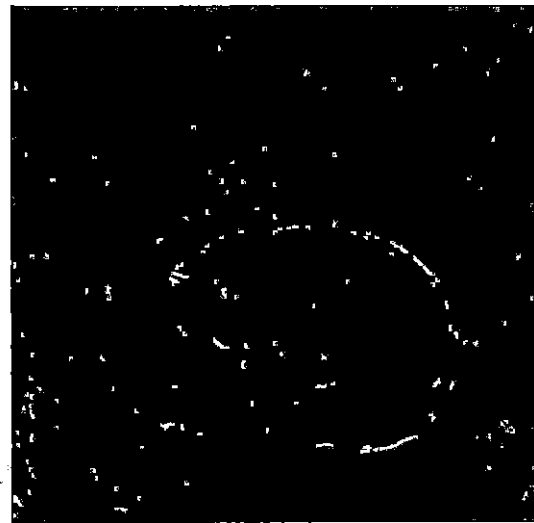
(a) Unregistered 2-D Beamline Images



(b) Registered 2-D Beamline Images

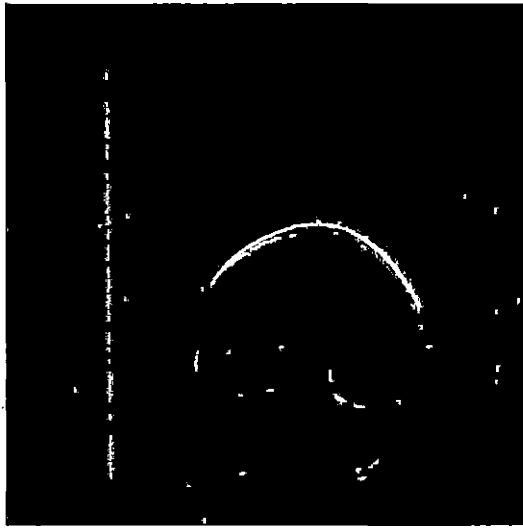


(c) Unregistered 2-D Orthogonal Images

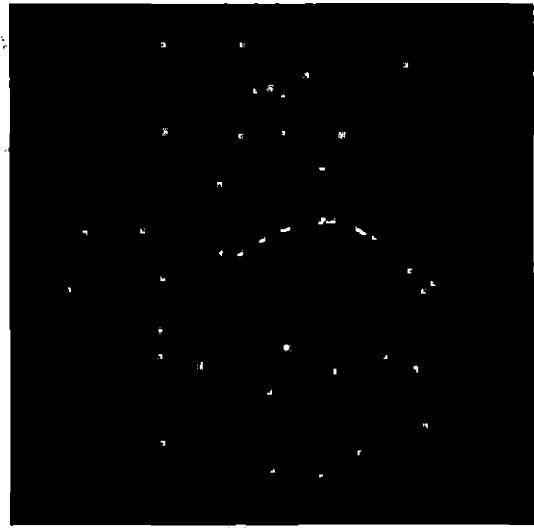


(d) Registered 2-D Orthogonal Images

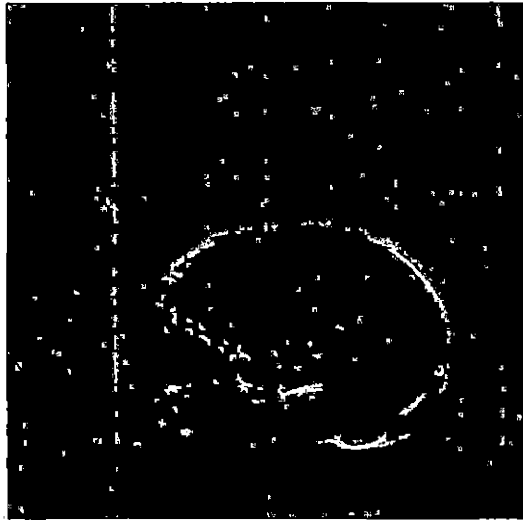
Fig. 4.6: Image Comparisons between Unregistered Images and Mutual Information Maximization Output



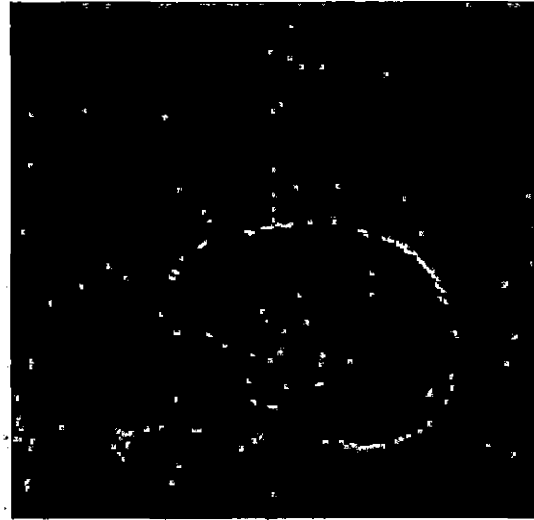
(a) Unregistered 2-D Beamline Images



(b) Registered 2-D Beamline Images

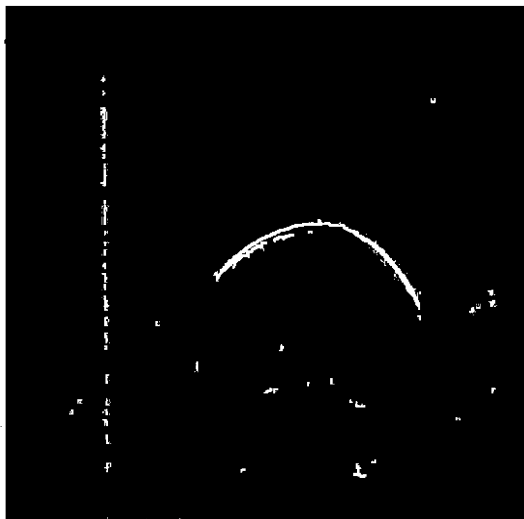


(c) Unregistered 2-D Orthogonal Images

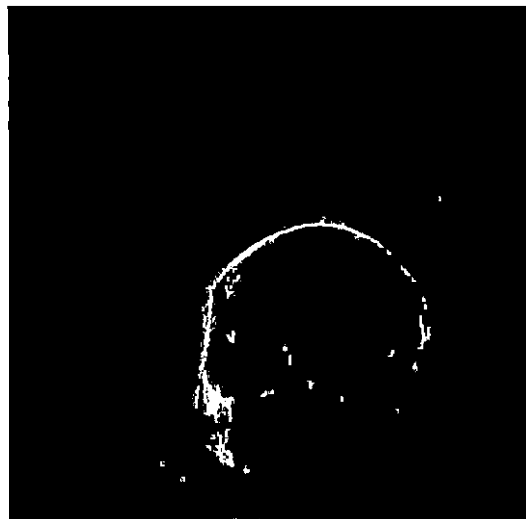


(d) Registered 2-D Orthogonal Images

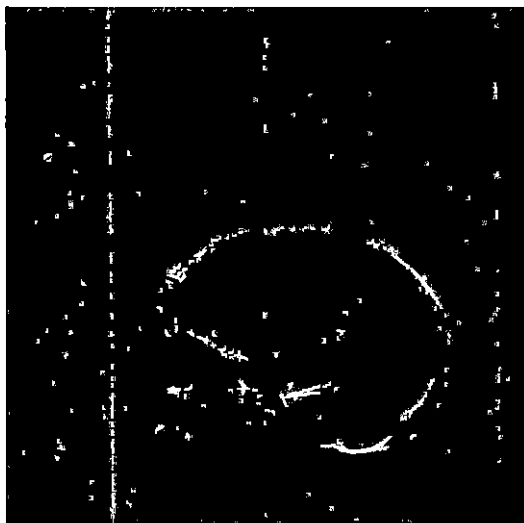
Fig. 4.7: Image Comparisons between Unregistered Images and Enhanced Correlation Coefficient Maximization Output



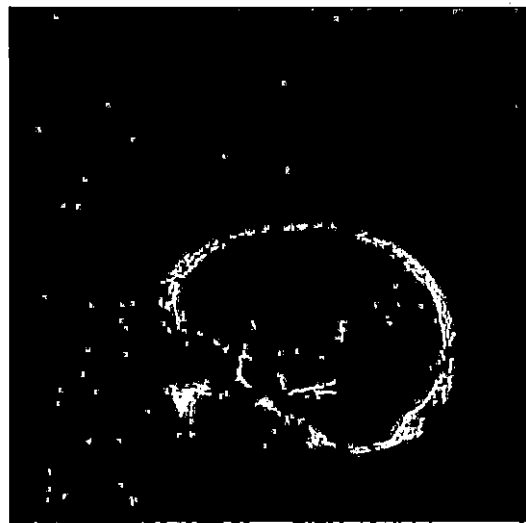
(a) Unregistered 2-D Beamline Images



(b) Registered 2-D Beamline Images



(c) Unregistered 2-D Beamline Images

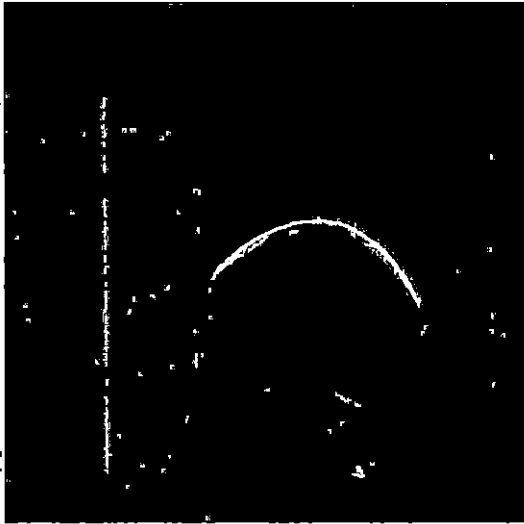


(d) Registered 2-D Beamline Images

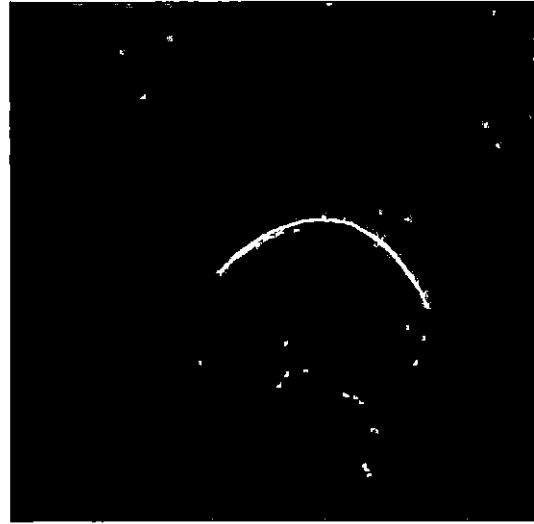
Fig. 4.8: Image Comparisons between Unregistered Images and Iterative Closest Point Output

in these images causing erroneous feature detection. Due to the point clouds for the reference and captured images being unmappable to each other, this algorithm failed to find the optimal alignments for both the beamline and orthogonal image sets.

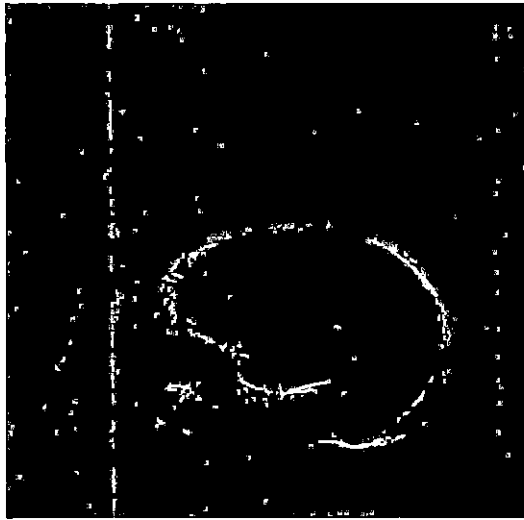
Figure 4.9 shows the final algorithm compared for this research. This is a non-rigid alignment metric and was unable to provide overall transformation results for the entire images, so no transformation results are shown in the next section. The visual comparisons are provided merely for completion. This algorithm has failed to perform any alignment step for either set of images, likely due to the large amount of noise.



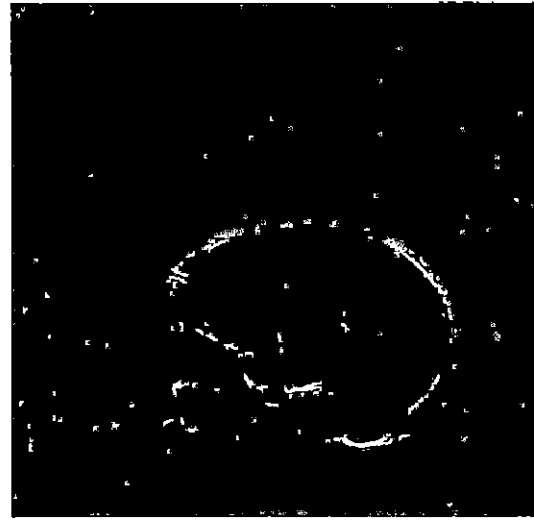
(a) Unregistered 2-D Beamline Images



(b) Registered 2-D Beamline Images



(c) Unregistered 2-D Orthogonal Images



(d) Registered 2-D Orthogonal Images

Fig. 4.9: Image Comparisons between Unregistered Images and Log-Domain Diffeomorphic Registration Output

4.3 Comparison of Results

Tab. 4.1: Alignment Results for Image Registration Methods

2-D Beamline	Expected	FFT	MI	ECC	ICP
Lateral (mm)			1.70 IN	0.32 IN	
Longitudinal (mm)					
Yaw (°)			0.83		
Execution (s)					
2-D Orthogonal	Expected	FFT	MI	ECC	ICP
Longitudinal (mm)		2.83 IN	2.83 IN	2.80 IN	
Vertical (mm)		0.86 DN	0.87 DN		
Pitch (°)					
Execution (s)					

Legend:

- Blue Expected value
- Green Less than or equal to 0.5 of expected value
- Yellow Less than or equal to 1.0 of expected value
- Red Greater than 1.0 of expected value

The results shown in Table 4.1 show the registration results of each algorithm and its respective run time. A legend is provided to note the range of each value with respect to the expected value. The expected values are given as a result of the manual process used for obtaining the reference and captured images of the skull phantom that were used for this thesis. Each algorithm was implemented using MATLAB and

its run time is calculated using MATLAB's built-in stopwatch timer. The angles of rotation are in degrees, the lateral and longitudinal shifts are in pixels, and the values of time are in seconds.

The results show that three registration methods—log-polar phase correlation, mutual information maximization, and enhanced correlation coefficient maximization—are either within the required goals of 0.5 mm with respect to translation and 0.5° with respect to rotation or otherwise reasonably accurate enough for further investigation before implementation. The iterative closest point algorithm failed on all accounts of alignment due to poor point cloud generation, and the log-domain diffeomorphic algorithm was unable to provide numeric transformation results over the whole image due to its method of mapping pixels between the two images rather than aligning the entire image. Also of note is the fact that all algorithms outperformed manual alignment in terms of completion time which provides a significant speed-up of the verification process.

5. SUMMARY OF FINDINGS

5.1 *Conclusions*

This thesis provides the groundwork for an automated patient alignment system using image registration techniques. Several methods were compared to determine the optimal registration techniques for implementation, including a phase correlation method [30], a mutual information maximization method [24, 29], an ECC maximization method [12], ICP methods [6, 18], and a diffeomorphic registration method [37] using Thirion's demon algorithm [36]. PDE-based methods were also considered [39, 38], but were not implemented for testing due to differences in application scope and image types.

The goal of this research is to determine the optimal patient alignment techniques using image registration to enhance current manual patient alignment methods. This will eliminate the need for fiducial markers which will significantly decrease the time before and during treatment as well as reduce the stress on the patient and reduce the risk of complications involved with the extra surgery and healing process.

Each algorithm was implemented on a personal laptop using the MATLAB environment. This is significant because implementing these algorithms on a dedicated system using a more efficient environment will provide further benefits to speed than those shown in this thesis. Test beamline and orthogonal images of a skull phantom

were taken at LLUMC and used for the input images for each registration algorithm. The captured images were manually transformed using known rotations and shifts, and these values were used to compare against the output of each algorithm to verify the alignment.

In conclusion, each image registration algorithm provided a significant increase in speed. While no single algorithm proved optimal in all cases of alignment, three of the algorithms demonstrate sufficient accuracy and performance to carry into further optimization and potential implementation. The phase correlation algorithm provided no value for rotation, likely due to errors in conversion from Cartesian coordinates to log-polar coordinates, and translation within the intended error of the expected values for registration of the beamline images, and within double the intended error for registration of the orthogonal images. This algorithm was optimal for overall translation and speed in comparison to the other algorithms. The roles of the mutual information maximization and ECC maximization algorithms appear to have switched for the beamline and orthogonal images, as the mutual information maximization algorithm performed better for the orthogonal images while the ECC maximization algorithm performed better for the beamline images. Finally, although the ICP algorithm performed faster than manual alignment, it was unable to provide accurate results for either rotation or translation based on the detected features within the images.

5.2 Recommendations for Implementation

Testing shows the practicality of various registration algorithms for patient alignment. Therefore, implementation should not rely on a single method. Instead, a number of potential options are available for effectively utilizing the top performing algorithms. A system of multiple processors, with each processor simultaneously running a separate algorithm, will allow for a more optimal alignment as different orientations of the patient may have different computation requirements. For example, a 2-D beamline image generally contains less noise and thus does not require as robust of an algorithm with respect to this type of artifact, while a 2-D orthogonal image contains a large amount of noise and will require an algorithm that is robust in the presence of quantum noise. The results of each algorithm could be compared in the treatment room, and the most optimal of these results used for verification. A potential drawback to this method, however, is that not all results would be available until all algorithms have completed execution, resulting in the overall process only being as fast as the slowest algorithm. A resolution to this issue is to halt execution of all algorithms once a single algorithm has met the minimum requirements for alignment.

Another viable option for implementation is to combine several algorithms to calculate the optimal alignment. For example, during tests of the 2-D beamline images, the phase correlation method was optimal for translation, while the enhanced correlation coefficient maximization method was optimal for rotation. Since the phase correlation method is invariant with respect to the order in which translation and rotation is registered, this method would be applied to find the difference in shift between the images. After the captured image is shifted back to its reference image, the

reference image and the shifted captured image would then be passed to the enhanced correlation coefficient maximization method to calculate the rotation.

5.3 *Future Research*

Before this research can be applied on actual patients, rigorous testing and optimization will be required. Once the physicians at LLUMC are satisfied with the results after testing is completed, the optimal image registration algorithms based on this thesis will be implemented into the alignment system and used during treatment. Once implemented, other centers can consider these techniques for implementation as no new hardware or software systems are required due to the standard use of 2-D imaging in patient alignment, meaning this research is applicable to all forms of radiosurgery and can be implemented at almost all radiosurgery centers.

Other methods for patient alignment are also available for further investigation. The use of 3-D imaging may provide benefits such as accuracy and robustness over 2-D imaging and can unlock the potential for other areas of localization. Axial rotation of the skull, the rotation of the skull about the neck as the axis, is another feature for patient alignment that can allow for further robustness. 3-D imaging with the additional measurement of time can also grant access to other areas of research, such as real-time alignment for moving structures such as the heart or lungs.

APPENDIX A
IMAGE REGISTRATION ALGORITHMS

A.1 Phase Correlation Using Log-Polar Coordinates

The phase correlation technique requires as input values a reference image and a captured image and outputs the calculated rotation and shift between the two images.

Algorithm 1 Log-polar phase correlation algorithm for image registration [30]

```
1: function LOGPOLARPHASECORRELATION(ref, cap)
2:   ref_filt  $\leftarrow$  HighPassFilter(ref)
3:   cap_filt  $\leftarrow$  HighPassFilter(cap)
4:   ref_fft  $\leftarrow$  FFT(ref_filt)
5:   cap_fft  $\leftarrow$  FFT(cap_filt)
6:   phase  $\leftarrow$  PhaseCorrelation(ref_fft, cap_fft)
7:   shift  $\leftarrow$  FindPeak(phase)
8:   ref_log  $\leftarrow$  LogPolar(ref_filt)
9:   cap_log  $\leftarrow$  LogPolar(cap_filt)
10:  ref_log_fft  $\leftarrow$  FFT(ref_log)
11:  cap_log_fft  $\leftarrow$  FFT(cap_log)
12:  phase  $\leftarrow$  PhaseCorrelation(ref_log_fft, cap_log_fft)
13:  [x, y]  $\leftarrow$  FindPeak(phase)
14:  rotation  $\leftarrow$  (360/YSize(ref) * y)
15:  return [rotation, shift]
```

A.2 Mutual Information Maximization

MATLAB ships with its own image registration algorithm using a Mutual information maximization metric. Due to its proprietary nature, the complete code is not readily available. The following is a basic calculation of mutual information between two vectors. This algorithm takes the reference and captured images as column vectors and outputs the mutual information shared between the vectors.

Algorithm 2 Mutual information maximization for image registration [24, 29]

```
1: function MUTUALINFORMATIONMAXIMIZATION(ref, cap)
2:   for i ← 1 to length(cap) do
3:     for j ← 1 to length(ref) do
4:        $distance_j \leftarrow (ref_{j,1} - cap_{i,1})^2 + (ref_{j,2} - cap_{i,2})^2$ 
5:        $mi_{i,j} \leftarrow \text{MarginalEntropy}(cap_i) + \text{MarginalEntropy}(ref_j) -$   

          $\text{JointEntropy}(cap_i, ref_j)$ 
6:   return mi
```

A.3 Enhanced Correlation Coefficient Maximization

The ECC maximization algorithm requires as inputs the reference and captured images, an integer denoting the maximum number of iterations, and a user decided threshold value to terminate the algorithm when the perturbations reach below this value. This algorithm outputs the transformation between the two images.

Algorithm 3 Enhanced correlation coefficient maximization algorithm [12]

```
1: function ECC(ref, cap, iter, thres)
2:    $i_r \leftarrow \text{ComputeZeroMeanNormVector}(ref)$ 
3:    $p_0 \leftarrow \text{InitializeParameters}()$ 
4:   for  $j \leftarrow 1$  to Iterations do
5:      $transform \leftarrow \text{ComputeTransformation}(ref, cap, p_{j-1})$ 
6:      $cap \leftarrow \text{Transform}(cap, transform)$ 
7:      $i_c \leftarrow \text{ZeroMeanNormVector}(cap)$ 
8:      $G \leftarrow \text{ComputeJacobian}(transform)$ 
9:      $\Delta p_j \leftarrow \text{ComputePerturbations}(i_r, i_c, G)$ 
10:     $p_j \leftarrow p_{j-1} + \Delta p_j$ 
11:    if  $\|\Delta p_j\| < thres$  then
12:      break
13:  return  $transform$ 
```

A.4 Iterative Closest Point Methods

The ICP algorithm requires the reference and captured images and a user selected threshold value to terminate the algorithm when the difference in mean square error reaches below this value. This algorithm outputs the rotation and shift between the two images.

Algorithm 4 Iterative closest point algorithm for image registration [18]

```
1: function ITERATIVECLOSESTPOINT(ref, cap, thres)
2:    $e' \leftarrow \infty$ 
3:   [rotation, shift]  $\leftarrow$  Initialize(ref, cap)
4:   repeat
5:      $e \leftarrow e'$ 
6:      $p' \leftarrow rotation * cap + shift$ 
7:     pairs  $\leftarrow$  NearestNeighborSearch(ref, cap')
8:     [rotation, shift]  $\leftarrow$  UpdateAlignment(ref, cap, pairs, rotation, shift)
9:      $e' \leftarrow$  RootMeanSquare(ref, cap, pairs)
10:  until  $|e' - e| < thres$ 
11:  return [rotation, shift]
```

A.5 Log-Domain Diffeomorphic Registration

The log-domain diffeomorphic registration algorithm requires the reference and captured images and an integer denoting the maximum number of iterations. This algorithm outputs the warped captured image.

Algorithm 5 Log-domain diffeomorphic image registration [37]

```
1: function DIFFEOMORPHICREGISTRATION(ref, cap, iter)
2:   tx  $\leftarrow$  0
3:   ty  $\leftarrow$  0
4:   [sy, sx]  $\leftarrow$  Gradient(ref)
5:   for i  $\leftarrow$  1 to iter do
6:     diff  $\leftarrow$  cap - ref
7:     ux  $\leftarrow$  -(diff * sx) / ((sx2 + sy2) + diff2)
8:     uy  $\leftarrow$  -(diff * sy) / ((sx2 + sy2) + diff2)
9:     tx  $\leftarrow$  tx + GaussianFilter(ux)
10:    ty  $\leftarrow$  ty + GaussianFilter(uy)
11:    cap  $\leftarrow$  MovePixels(cap, tx, ty)
12:  return cap
```

APPENDIX B
INTERPOLATION ALGORITHMS

B.6 Nearest Neighbor Interpolation

Below is a nearest neighbor interpolation algorithm for image resampling. This algorithm requires a set of discrete points, an initial width and height, and a specified width and height to which the image will be scaled. The output of this algorithm is the resized image.

Algorithm 6 Nearest neighbor interpolation used for image resampling [1]

```
1: function NEARESTNEIGHBORINTERPOLATION(img, w1, h1, w2, h2)
2:   temp  $\leftarrow w2 * h2$ 
3:   x_ratio  $\leftarrow w1/w2$ 
4:   y_ratio  $\leftarrow h1/h2$ 
5:   for i  $\leftarrow 1$  to h2 do
6:     for j  $\leftarrow 1$  to w2 do
7:       px  $\leftarrow \text{Floor}(j * x\_ratio)$ 
8:       py  $\leftarrow \text{Floor}(i * y\_ratio)$ 
9:       tempi*w2+j  $\leftarrow \text{img}$ py*w1+px
10:  return temp
```

B.7 Linear Interpolation

Linear interpolation requires the x and y values of two points and the desired x value to be interpolated. The output value is the y value corresponding to the input x value.

Algorithm 7 Linear interpolation [1]

```
1: function LINEARINTERPOLATION( $x_1, y_1, x_2, y_2, x$ )  
2:   return  $y_1 + (y_2 - y_1)/(x_2 - x_1) * (x - x_1)$ 
```

B.8 Cubic Interpolation

Cubic interpolation requires four points and a desired x value to be interpolated. The output value is the y value corresponding to the input x value.

Algorithm 8 Cubic interpolation [1]

```
1: function CUBICINTERPOLATION( $p_0, p_1, p_2, p_3, x$ )  
2:    $a_0 \leftarrow p_3 - p_2 - p_0 + p_1$   
3:    $a_1 \leftarrow p_0 - p_1 - a_0$   
4:    $a_2 \leftarrow p_2 - p_0$   
5:    $a_3 \leftarrow p_1$   
6:   return  $a_0 * x^3 + a_1 * x^2 + a_2 * x + a_3$ 
```

APPENDIX C
NEAREST NEIGHBOR SEARCH ALGORITHMS

C.9 Exhaustive Search

The exhaustive nearest neighbor search algorithm is a naive algorithm that requires two sets of points, one based on the features of the reference image and the other based off the features of the captured image. This algorithm outputs a list of all closest pairs between the two sets.

Algorithm 9 Brute force algorithm for calculating closest points [18]

```
1: function BRUTEFORCE(ref, cap)
2:   for i ← 1 to length(cap) do
3:     for j ← 1 to length(ref) do
4:        $distance_j \leftarrow (ref_{j,1} - cap_{i,1})^2 + (ref_{j,2} - cap_{i,2})^2$ 
5:        $pairs_i \leftarrow \text{Min}(distance)$ 
6:   return pairs
```

C.10 Delauney Triangulation

Delaunay triangulation requires an input list of points to construct the Delaunay triangulation and outputs a list of edges of the triangles.

Algorithm 10 Build Delaunay Triangulation for nearest neighbor search [11]

```
1: function DELAUNEYTRIANGULATION(points)
2:   for i ← 1 to length(points) do
3:     triangle ← Surrounding(i)
4:     new_points ← CreatePointList()
5:     new_points.add(Edges(triangle))
6:     for j ← 1 to length(new_points) do
7:       if IsNotDelaunayTriangulation(j) then
8:         new_points.add(Edges(Flip(j)))
9:   return new_points
```

C.11 K-D Trees

The algorithm for construction of a K-D tree requires a list of points and a depth used to calculate the axis. This algorithm is iterative, so while it only outputs an individual node with a left child and a right child, each child has its own children which are connected to the root node through its parent node.

Algorithm 11 Build K-D tree for nearest neighbor search [5, 14]

```
1: function BUILDKDTree(points, depth)
2:   axis  $\leftarrow$  depth mod k
3:   median  $\leftarrow$  GetMedian(points)
4:   node  $\leftarrow$  CreateNode(median)
5:   node.left_child  $\leftarrow$  BuildKDTree(points0...median, depth + 1)
6:   node.right_child  $\leftarrow$  BuildKDTree(pointsmedian...points.size, depth + 1)
7:   return node
```

APPENDIX D
FEATURE DETECTION ALGORITHMS

D.12 Harris Corner Detector

The Harris corner detector requires an image input, a Gaussian window w , an arbitrary constant k , and an intensity threshold used for the corner detection. This algorithm outputs the non-maximal suppression of the matrix containing the feature points.

Algorithm 12 Harris Corner Detector [15]

```
1: function HARRISCORNERDETECTION( $img, w, k, thres$ )
2:    $img_x \leftarrow (\frac{\partial img}{\partial x}) \otimes w$ 
3:    $img_y \leftarrow (\frac{\partial img}{\partial y}) \otimes w$ 
4:    $img_{x2} \leftarrow (img_x)^2$ 
5:    $img_{y2} \leftarrow (img_y)^2$ 
6:    $img_{xy} \leftarrow img_x * img_y$ 
7:    $m \leftarrow \begin{pmatrix} img_{x2} & img_{xy} \\ img_{xy} & img_{y2} \end{pmatrix}$ 
8:    $det \leftarrow (img_{x2} * img_{y2} - img_{xy}^2)$ 
9:    $trace \leftarrow img_{x2} + img_{y2}$ 
10:   $r \leftarrow det - k * trace^2$ 
11:  for  $i \leftarrow 1$  to XSize( $r$ ) do
12:    for  $j \leftarrow 1$  to YSize( $r$ ) do
13:      if  $r_{x,y} < thres$  then
14:         $r_{x,y} \leftarrow 0$ 
15:  return ( $eig_{min} == r_{max}$ )& $r$ ;
```

D.13 Shi & Tomasi's Minimum Eigenvalue Method

Similar to the Harris corner detector, the Shi & Tomasi minimum eigenvalue method requires an image input, a Gaussian window w , an arbitrary constant k , and an intensity threshold used for the corner detection. This algorithm also outputs the non-maximal suppression of the matrix containing the feature points.

Algorithm 13 Shi & Tomasi's Minimum Eigenvalue Method [33]

```
1: function SHITOMASICORNERDETECTION( $img, w, k, thres$ )
2:    $img_x \leftarrow (\frac{\partial img}{\partial x}) \otimes w$ 
3:    $img_y \leftarrow (\frac{\partial img}{\partial y}) \otimes w$ 
4:    $img_x2 \leftarrow (img_x)^2$ 
5:    $img_y2 \leftarrow (img_y)^2$ 
6:    $img_{xy} \leftarrow img_x * img_y$ 
7:    $m \leftarrow \begin{pmatrix} img_x2 & img_{xy} \\ img_{xy} & img_y2 \end{pmatrix}$ 
8:   for  $i \leftarrow 1$  to XSize( $img$ ) do
9:     for  $j \leftarrow 1$  to YSize( $img$ ) do
10:        $eigs_{x,y} \leftarrow \text{Min}(\text{Eigenvalues}(m))$ 
11:        $r_{x,y} \leftarrow (eigs_{x,y} > thres * \text{Max}(mins_{x,y}))$ 
12:     for  $i \leftarrow 1$  to XSize( $r$ ) do
13:       for  $j \leftarrow 1$  to YSize( $r$ ) do
14:         if  $r_{x,y} < thres$  then
15:            $r_{x,y} \leftarrow 0$ 
16:   return ( $mins == r_{max}$ ) &  $r$ 
```

D.14 FAST Corner Detector

The FAST corner detector requires an input image and an intensity threshold and outputs a matrix of the detected corners from the input image.

Algorithm 14 FAST corner detector [31]

```
1: function FASTCORNERDETECTOR(img, thres)
2:   for i ← 4 to YSize(img) - 4 do
3:     for j ← 4 to XSize(img) - 4 do
4:       center ← [i, j]
5:       radius ← 4
6:       circ ← Circle(center, radius)
7:       counter ← 0
8:       for each point in circ do
9:         if point < thres then
10:           counter ← counter + 1
11:       if counter ≥ 12 then
12:         cornersi,j ← 1
13:   return corners
```

REFERENCES

- [1] Milton Abramowitz and Irene A. Stegun, editors. *Handbook of Mathematical Functions: With Formulas, Graphs, and Mathematical Tables*, volume 55. Dover Publications, 1964.
- [2] Simon Baker and Iain Matthews. Lucas-kanade 20 years on: A unifying framework. *International Journal of Computer Vision*, 56(3):221–255, February 2004.
- [3] Ma Consuelo Bastida-Jumilla, Jorge Larrey-Ruiz, Rafael Verdú-Monedero, Juan Morales-Sánchez, and José-Luis Sancho-Gómez. Ddr and portal image registration for automatic patient positioning in radiotherapy treatment. *Journal of Digital Imaging*, 24(2):999–1009, December 2011.
- [4] Rachid Belaroussi and Guillaume Morel. Combination of image registration algorithm for patient alignment in proton beam therapy. In Abderrahim Elmoataz, Olivier Lezoray, Fathallah Nouboud, and Driss Mammass, editors, *Image and Signal Processing*, Lecture Notes in Computer Science, pages 183–191. Springer Berlin Heidelberg, Cherboung-Octeville, France, July 2008.
- [5] Jon Louis Bentley. Multidimensional binary search trees used for associative searching. *Communications of the ACM*, 18(9):509–517, September 1975.
- [6] P. J. Besl and Neil D. McKay. A method for registration of 3-d shapes.

- IEEE Transactions on Pattern Analysis and Machine Intelligence*, 14(2):239–256, February 1992.
- [7] D. K. Bewley. The 8 mev linear accelerator at the mrc cyclotron unit hammer-smith hospital, london. *British Journal of Radiology*, 58(687):213–217, March 1985.
- [8] Mainak Biswas and Truong Nguyen. A novel motion estimation algorithm using phase plane correlation for frame rate conversion. In Michael B. Matthews, editor, *Conference Record of the Thirty-Sixth Asilomar Conference on Signals, Systems, and Computers*, volume 1, pages 492–496, Pacific Grove, California, USA, November 2002. IEEE.
- [9] Lisa Gottesfeld Brown. A survey of image registration techniques. *ACM Computing Surveys*, 24(4):325–276, August 1992.
- [10] Australian National Proton Facility Steering Committee. Australian national proton facility discussion paper, 2001.
- [11] B Delaunay. Sur la sphere vide. *Izvestia Akademii Nauk SSSR, Otdelenie Matematicheskikh i Estestvennykh Nauk*, 7:793–800, 1934.
- [12] Georgios D. Evangelidis and Emmanouil Z. Psarakis. Parametric image alignment using enhanced correlation coefficient maximization. *IEEE Transactions on Pattern Analysis and Machine Intelligence*, 30(10):1858–1865, October 2008.
- [13] Martin A. Fischler and Robert C. Bolles. Random sample consensus: A paradigm for model fitting with applications to image analysis and automated cartography. *Communications of the ACM*, 24(6):381–395, June 1981.

- [14] Jerome H Friedman, Jon Louis Bentley, and Raphael Ari Finkel. An algorithm for finding best matches in logarithmic expected time. *ACM Transactions on Mathematical Software (TOMS)*, 3(3):209–226, September 1977.
- [15] Chris Harris and Mike Stephens. A combined corner and edge detector. In C. J. Taylor, editor, *Proceedings of the Alvey Vision Conference*, volume 15, pages 147–152, Manchester, England, September 1988. Alvey Vision Club.
- [16] John O. Archangeau James M. Slater, Daniel W. Miller. development of a hospital-based proton beam treatment center. *International Journal of Radiation Oncology * Biology * Physics*, 14(4):761–775, April 1988.
- [17] Yoon-Jong kim, Dong-Hoon Lee, and Seung-Hong Hong. A study on portal image for the automatic verification of radiation therapy. *IEICE TRANSACTIONS on Fundamentals of Electronics, Communications and Computer Sciences*, 82(6):945–951, June 1999.
- [18] Hans Martin Kjer and Jakob Wilm. Evaluation of surface registration algorithms for pet motion correction. Bachelor thesis, Technical University of Denmark, Kongens Lyngby, Denmark, June 2010.
- [19] Lars Leksell. The stereotaxic method and radiosurgery of the brain. *Acta Chirurgica Scandinavica*, 102(4):316–319, December 1951.
- [20] Richard P. Levy and Reinhard W. M. Schulte. Stereotactic radiosurgery with charged-particle beams: Technique and clinical experience. *Translational Cancer Research*, 1(2):159–172, October 2012.

- [21] Richard P. Levy, Reinhard W. M. Schulte, Jerry D. Slater, Dan W. Miller, and James M. Slater. Stereotactic radiosurgery—the role of charged particles. *Acta Oncologica*, 38(2):165–169, October 1999.
- [22] Bruce D. Lucas and Takeo Kanade. An iterative image registration technique with an application to stereo vision. In Ann Drinan, editor, *Proceedings of the 7th International Joint Conference on Artificial Intelligence*, volume 2 of *International Joint Conference on Artificial Intelligence*, pages 674–679, University of British Columbia Vancouver, B.C., Canada, August 1981. The International Joint Conferences on Artificial Intelligence, Inc., Morgan Kaufmann Publishers Inc.
- [23] J. B. Antoine Maintz and Max A. Viergever. An overview of medical image registration methods. Technical report, In Symposium of the Belgian Hospital Physicists Association – SBPH-BVZF, 1996.
- [24] David Mattes, David R. Haynor, Hubert Vesselle, Thomas K. Lewellyn, and William Eubank. Nonrigid multimodality image registration. In Milan Sonka and Kenneth M. Hanson, editors, *Medical Imaging 2001: Image Processing*, volume 4322 of *Proceedings of SPIE*, pages 1609–1620, San Diego, California, USA, July 2001. SPIE, SPIE Publications.
- [25] F. Mills. Technical assessment of the loma linda university proton accelerator. Technical report, Fermi National Accelerator Laboratory, Batavia, Illinois, USA, October 1989.
- [26] Hans P. Moravec. *Obstacle Avoidance and Navigation in the Real World by a*

- Seeing Robot Rover*. PhD thesis, Stanford University, Stanford, California, USA, September 1980.
- [27] Pinar Muyan-Ozcelik, John D. Owens, Junyi Xia, and Sanjiv S. Samant. Fast deformable registration on the gpu: A cuda implementation of demons. In Osvaldo Gervasi, Beniamino Murgante, Antonio Lagan, David Taniar, and Youngsong Mun, editors, *International Conference on Computational Sciences and Its Applications, 2008 – ICCSA 2008*, pages 223–233, Perugia, Italy, 2008. IEEE.
- [28] Chuck Palahniuk. *Invisible Monsters*. W. W. Norton & Company.
- [29] Smriti Raghunathan, Don Stedney, P. Schmalbrock, and Bradley D. Clymer. Image registration using rigid registration and maximization of mutual information, 2005.
- [30] B. Srinivasa Reddy and B. N. Chatterji. An fft-based technique for translation, rotation and scale-invariant image registration. *IEEE Transactions on Image Processing*, 5(8):1266–1271, August 1996.
- [31] Edward Rosten and Tom Drummond. Fusing points and lines for high performance tracking. In *Tenth IEEE International Conference on Computer Vision – ICCV 2005*, volume 2, pages 1508–1511, Beijing, People’s Republic of China, October 2005. IEEE.
- [32] Edward Rosten and Tom Drummond. Machine learning for high-speed corner detection. In Ale Leonardis, Horst Bischof, and Axel Pinz, editors, *Computer Vision – ECCV 2006*, volume 3951 of *Lecture Notes in Computer Science*, pages 430–443. Springer Berlin Heidelberg, Graz, Austria, May 2006.

- [33] Jianbo Shi and Carlo Tomasi. Good features to track. In *Proceedings of the IEEE Conference on Computer Vision and Pattern Recognition – CVPR 1994*, pages 593–600, Seattle, Washington, USA, June 1994. IEEE.
- [34] Perry Sprawls. *Physical Principles of Medical Imaging*. Medical Physics Publishing, Madison, Wisconsin, USA, 2nd edition edition, May 1995.
- [35] Inc. The MathWorks. Image processing toolbox for matlab, 2012.
- [36] J. P. Thirion. Image matching as a diffusion process: An analogy with maxwell’s demons. *Medical Image Analysis*, 2(3):243–260, April 1998.
- [37] Tom Vercauteren, Xavier Pennec, Aymeric Perchant, and Nicholas Ayache. Symmetric log-domain diffeomorphic registration: A demons-based approach. In Dimitris Metaxas, Leon Axel, Gabor Fichtinger, and Gbor Szekely, editors, *Medical Image Computing and Computer-Assisted Intervention – MICCAI 2008*, volume 5242 of *Lecture Notes in Computer Science*, pages 754–761. Springer Berlin Heidelberg, New York City, New York, USA, September 2008.
- [38] Joachim Weickert. *Anisotropic Diffusion in Image Processing*. ECMI. Teubner-Verlag, Stuttgart, Germany, 1998.
- [39] Joachim Weickert. Efficient image segmentation using partial differential equations and morphology. *Pattern Recognition*, 34(9):1813–1824, September 2001.
- [40] Robert R. Wilson. Radiological use of fast protons. *Radiology*, 47(5):487–491, July 1946.